VIROLOGY

SARS-related coronavirus S-protein structures reveal synergistic RBM interactions underpinning high-affinity human ACE2 binding

Jingjing Wang[1]†, Yong Ma[1]†, Zimu Li[1,2,3], Hang Yuan[1,4], Banghui Liu[1], Zexuan Li[1,4], Mengzhen Su[1,5], Gul Habib[1], Yutong Liu[1], Lutang Fu[6], Peiyi Wang[6], Mei Li[2], Jun He[1], Jing Chen[2], Peng Zhou[2], Zhengli Shi[2]*, Xinwen Chen[2]*, Xiaoli Xiong[1]*

High-affinity and specific binding toward the human angiotensin-converting enzyme 2 (hACE2) receptor by severe acute respiratory syndrome coronavirus (SARS)–related coronaviruses (SARSr-CoVs) remains incompletely understood. We report cryo–electron microscopy structures of eight different S-proteins from SARSr-CoVs found across Asia, Europe, and Africa. These S-proteins all adopt tightly packed, locked, prefusion conformations. These structures enable the classification of SARSr-CoV S-proteins into three types, based on their receptor-binding motif (RBM) structures and ACE2 binding characteristics. Type-2 S-proteins often preferentially bind bat ACE2 (bACE2) over hACE2. We report a structure of a type-2 BtKY72-RBD in complex with bACE2 to understand ACE2 specificity. Structure-guided mutagenesis of BtKY72-RBD reveals that multiple synergistic mutations in four different regions of RBM are required to achieve high-affinity hACE2 binding. Similar RBM changes can also confer hACE2 binding to another type-2 BM48-31 S-protein, which is primarily non-ACE2 binding. These results provide an understanding of how high-affinity hACE2 binding may be acquired by SARSr-CoV S-proteins.

INTRODUCTION

Severe acute respiratory syndrome coronavirus (SARS-CoV) (*1*–*4*) and severe acute respiratory syndrome coronavirus 2 (SARS-CoV-2) (*5*–*9*) have crossed the species barrier to infect humans. Both SARS-CoV and SARS-CoV-2 have been identified to use their spike (S) proteins on the virus surface to bind human angiotensin-converting enzyme 2 (hACE2) as the receptor to enter human cells (*5*, *10*). The coronavirus S-proteins are large, heavily glycosylated, type I, homotrimeric, viral membrane fusion proteins (*11*). They can be functionally divided into two parts: the S1 part, responsible for cell attachment, and the S2 part, facilitating membrane fusion (*12*, *13*). For SARS-CoV and SARS-CoV-2, their S1 parts contain the N-terminal domain (NTD), receptor binding domain (RBD), Domain C, and Domain D. Of these, the RBD specifically binds to hACE2. A large number of SARS-CoV (*14*–*19*) and SARS-CoV-2 (*20*–*24*) S-trimer prefusion structures have been determined, showing dynamics with RBDs in "up" and "down" positions, which correspond to the "open" and "closed" conformations, respectively. A more compact "locked" prefusion conformation, with all three RBDs in "down" positions and ordered fusion peptide proximal region (FPPR), has been further identified in a few studies for SARS-CoV, SARS-CoV-2, and certain SARS-related coronavirus S-trimers (*16*, *24*–*30*). When the RBD is in a "down" position within an S-trimer, its ACE2 interaction interface is largely obstructed sterically; therefore, RBDs must adopt an "up" position to interact with the ACE2 receptor (*14*, *15*, *17*, *20*, *31*). We and others propose that the transition of RBDs from the "down" to the "up" position within an S-trimer, mediated via ACE2 binding, triggers the S-trimer to undergo a fusogenic structural transition (*20*, *31*).

Because of SARS-CoV and SARS-CoV-2's impacts on public health, numerous studies have been conducted in various attempts to understand their ecology. These efforts have led to the identification of a considerable number of coronaviruses genetically related to SARS-CoV and SARS-CoV-2 in horseshoe bats (genus *Rhinolophus*) (*32*–*36*). These bat coronaviruses form the species *SARS-related coronavirus* (SARSr-CoVs), and along with SARS-CoV and SARS-CoV-2, forming the *Sarbecovirus* subgenus, within the *Betacoronavirus* genus of the *Coronaviridae* family (https://ictv.global/taxonomy). With the increased identification of bat SARSr-CoVs, it is now understood that horseshoe bats likely serve as the natural host of SARSr-CoVs, from which spillover may occur to infect other animals, including civets, pangolins, and humans (*33*, *34*, *37*, *38*). A high diversity of coronavirus species has been identified in Rhinolophidae bats captured not only in Asia, including China, Japan, Laos, and Cambodia, but also in Europe and Africa (*37*, *39*–*46*). Phylogenetic classification of SARSr-CoVs, based on their S-RBD sequences, has led to the definition of multiple clades (*47*–*49*): clade 1a (e.g., SARS-CoV), clade 1b (e.g., SARS-CoV-2), clade 1c (e.g., BtKY72), and clade 2 (e.g., GX2013) (*50*). Clade 1a and 1b SARSr-CoV strains, such as BatCoV-WIV1, BANAL-20-52, and BANAL-20-236, have been shown to use hACE2 to mediate infection (*33*, *40*). Clade 2 strains, including RmYN02, YN2013, GX2013, and HeB2013 (*51*, *52*), with two loops deleted in the RBD and unidentified receptors, are unable to bind either hACE2 or bat ACE2 (bACE2). Last, clade 1c strains with deletions in only one RBD loop have been shown to have varied abilities in using ACE2. It has been identified that BtKY72 (*53*) S-protein binds *Rhinolophus affinis* ACE2 (*Ra*ACE2) with no hACE2 binding ability. The mechanism underlying the specificity in ACE2 utilization remains incompletely understood.

[1]State Key Laboratory of Respiratory Disease, Guangdong Provincial Key Laboratory of Stem Cell and Regenerative Medicine, Guangdong-Hong Kong Joint Research Laboratory for Stem Cell and Regenerative Medicine, Guangzhou Institutes of Biomedicine and Health, Chinese Academy of Sciences, Guangzhou, China. [2]Guangzhou National Laboratory, Guangzhou, Guangdong, China. [3]Graduate School of Guangzhou Medical University, Guangzhou, China. [4]University of Chinese Academy of Sciences, Beijing, China. [5]University of Science and Technology of China, Hefei, China. [6]Cryo-electron Microscopy Center, Southern University of Science and Technology, Shenzhen, China.
*Corresponding author. Email: shi_zhengli@gzlab.ac.cn (Z.S.); chen_xinwen@gzlab.ac.cn (X.C.); xiong_xiaoli@gibh.ac.cn (X.X.)
†These authors contributed equally to this work.

Here, we report cryo–electron microscopy (cryo-EM) structures of eight SARSr-CoV S-trimers. All these S-trimers adopt RBD "down" locked prefusion conformations without exhibiting conformational dynamics observed for SARS-CoV and SARS-CoV-2 S-trimers. We further report a cryo-EM structure of the complex formed between BtKY72-RBD and a bat ACE2 ($bACE2_{Ra9479}$). Through site-directed mutagenesis, guided by the BtKY72-RBD:bACE2 structure, we elucidate how high-affinity hACE2 binding, comparable to that of SARS-CoV-2, can be conferred to the BtKY72 S-protein through the modification of four key molecular determinants within the RBD receptor-binding motif (RBM). We confirm that similar RBM modifications can also confer hACE2 binding to the SARSr-CoV BM48-31 (*54*) S-protein, which, in its native form, exhibits almost non-ACE2 binding. We further demonstrate that ACE2 binding affinity is generally correlated to the cell fusion activity mediated by the S-proteins, suggesting that receptor binding plays a key role for SARSr-CoV S-proteins in mediating efficient cell invasion.

RESULTS

Cryo-EM structures of S-proteins from eight SARSr-CoVs

To better understand the SARSr-CoV S-protein structure, we constructed a phylogenetic tree based on an S-protein sequence alignment (Fig. 1A). We selected representative S-proteins from various clades, curating S-proteins from eight different SARSr-CoV strains isolated from bats of different geographical regions. They are bat coronavirus BtKY72 (*Rhinolophus* spp.), BM48-31/2008 BGR/2008 (*Rhinolophus blasii*), BANAL-20-52 (*Rhinolophus malaynus*), BANAL-20-236 (*Rhinolophus marshalli*), YN2013 (*Rhinolophus ferrumequinum*), RmYN02 (*Rhinolophus malaynus*), GX2013 (*Rhinolophus sinicus*), and HeB2013 (*Rhinolophus ferrumequinum*) (Fig. 1B). Among these SARSr-CoVs, BtKY72 was detected from Kenya, Africa; BM48-31 was detected in Bulgaria, Eastern Europe; BANAL-20-52 and BANAL-20-236 are from Laos, Southeast Asia; YN2013 and RmYN02 are from Yunnan, South China; GX2013 is from Guangxi, South China; and last, HeB2013 is from Hebei, North China (Fig. 1D). By comparison with the SARS-CoV-2 S sequence, 72.8 to 98.7% amino acid identities are found for the eight SARSr-CoV S-proteins. We determined cryo-EM structures of the above S-trimers at overall resolutions in the range of 2.5 to 3.8 Å (Fig. 1, figs. S1 to S3, and table S1). Notably, none of the bat SARSr-CoV S-proteins contains a polybasic furin cleavage site. The RmYN02 S-protein was identified to contain a three–amino acid residue (PAA) insertion at the S1/S2 cleavage site (*52*).

SARSr-CoV S-proteins all adopting an RBD-down locked prefusion conformation

All determined SARSr-CoV S-trimer structures adopt three RBD-down conformations. Superposition of the determined S-trimer structures onto the SARS-CoV-2 locked-2 conformation S-trimer structure [Protein Data Bank (PDB): 7XU2] gives RMSD (root mean square deviation) values (calculated for S-trimer pairs) lower than 1.5 Å for BtKY72 [0.819 Å; amino acid (AA)-ID: 72.78%], BM48-31 (0.811 Å; AA-ID: 72.81%), BANAL-20-52 (1.000 Å; AA-ID: 98.74%), BANAL-20-236 (1.216 Å; AA-ID: 91.14%), YN2013 (0.967 Å; AA-ID: 77.79%), RmYN02 (1.343 Å; AA-ID: 75.39%), GX2013 (1.272 Å; AA-ID: 77.14%), and HeB2013 (1.310 Å; AA-ID: 75.42%), respectively (amino acid sequence identities to the SARS-CoV-2 full-length S-protein are quoted). The intersubunit distances, as measured between T500 located near the apex of each SARS-CoV-2 S-protomer, are 10.3 Å for the locked conformations and 16.9 Å for the closed conformation (fig. S4, I and J). By comparison, the equivalent distances in the region of 9.1 to 12.7 Å are found for the determined SARSr-CoV S-trimer structures, suggesting that all determined S-trimer structures are in locked conformations (fig. S4). Superposition of the SARSr-CoV S-protomer structures to the SARS-CoV-2 S-protomer structure in closed conformation reveals that the RBD domains within the SARSr-CoV S-proteins are obviously more packed toward the NTD (fig. S5); such observation is consistent with SARSr-CoV S-proteins adopting locked conformations with more compact trimeric quaternary structures (fig. S4).

Domain D has been identified to exhibit conformational dynamics in both SARS-CoV and SARS-CoV-2 S-trimers. S-trimers in locked-1 and locked-2 conformations differ from each other primarily in the structure of Domain D. In the "locked-1" conformation, Domain D is rigidified with a large, disordered Domain D-loop, whereas in the "locked-2" conformation, Domain D is rigidified with the Domain D-loop fully ordered (*24*, *28*, *55*, *56*). As the eight determined SARSr-CoV S-trimer structures all adopt the "locked-2" conformation, their Domain D-loop regions adopt ordered-folded structures similar to that in the "locked-2" SARS-CoV-2 S-trimer. The folded Domain D structures in the eight S-trimers are stabilized by the cation-π interactions equivalent to that formed between Domain D residue $W633_{SARS2}$ (SARS2 subscript stands for SARS-CoV-2 S-protein numbering) and $R319_{SARS2}$ of the Domain C-D hinge region in the locked-2 SARS-CoV-2 S-trimer structure (fig. S6, A to I). The equivalent stabilizing interaction has also been found in the locked-2 SARS-CoV S-trimer structures (*16*). BM48-31 and BtKY72 S-proteins each have a two–amino acid insertion at the same position in Domain D (after the $S640_{SARS2}$). As a result, BM48-31 and BtKY72 Domain D structures show bulges toward the Domain D-loop C termini, compared with the "locked-2" SARS-CoV-2 S-trimer structure (fig. S6, A, B, I, and J).

Despite that the eight S-trimer structures all adopt the "locked-2" structure, the FPPRs adjacent to Domain D exhibit structural dynamics (Fig. 2 and fig. S6). The FPPR region is disordered in the RmYN02 S-trimer (Fig. 2F and fig. S6F). In the other seven SARSr-CoV S-trimer structures, the FPPR regions are mostly ordered (Fig. 2A and fig. S6, A to E and G to H); a recent study shows that the FPPR region reaches the surface of the host-cell membrane after SARS-CoV-2 S-protein completes its fusogenic structural transition (*57*). The conformation dynamics observed among these eight SARSr-CoV S-trimer structures in or around the Domain D region (Fig. 2 and fig. S6) may affect S-protein activity, considering that proteolytic cleavage in Domain Ds of SARS-CoV and SARS-CoV-2 S-proteins was found to modulate S-protein activity (*58*).

Binding of small molecules by the SARSr-CoV S-trimers

Binding of linoleic acid (LA) in SARS-CoV and SARS-CoV-2 RBDs has been proposed to stabilize locked S-trimer structures, by mediating interactions between two neighboring RBDs (*16*, *25*, *26*). LAs have also been observed in the RBDs of the locked Guangxi pangolin CoV S-trimer (*26*). Among the determined locked SARSr-CoV S-trimer structures, densities compatible with LAs are only found to occupy the hydrophobic fatty acid binding pockets in the RBDs of BM48-31 and BANAL-20-52 S-trimers (Fig. 2, B and C). Notably, a

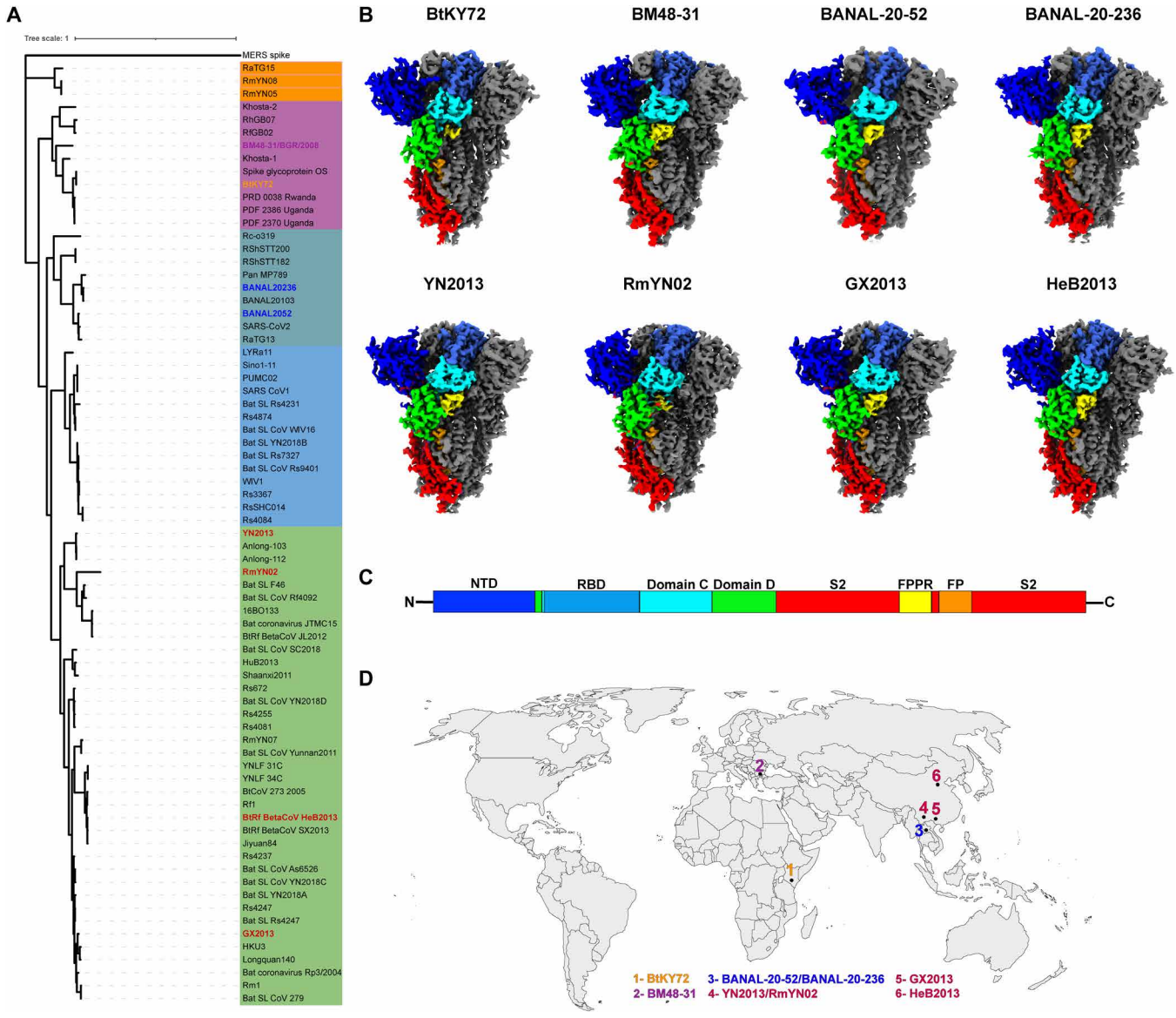

Fig. 1. Cryo-EM structures of S-trimers from eight SARSr-CoVs of different geographical regions. (**A**) Phylogenetic tree constructed based on 73 sarbecovirus S-protein amino acid sequences, with MERS S-protein used as the outgroup. The tree shows the evolutionary relationships and genetic clustering based on sequence similarities. (**B**) Cryo-EM densities showing the overall architectures of the S-trimers of BtKY72, BM48-31, BANAL-20-52, BANAL-20-236, YN2013, RmYN02, GX2013, and HeB2013 SARSr-CoV strains. Each S-trimer is shown with one of the featured protomer colored according to the scheme in (C), and the other protomers are colored in gray. (**C**) A schematic representation illustrates the domain organization of SARSr-CoV S-protein, showing eight functional domains or regions: NTD (amino acids 13 to 307), RBD (amino acids 330 to 528), Domain C (amino acids 320 to 330 and 529 to 592), Domain D (amino acids 308 to 319 and 593 to 699) in S1 (amino acids 1 to 699) and FPPR (amino acids 834 to 856), and fusion peptide (FP; amino acids 866 to 910) in S2 (amino acids 700 to 1273). Domain boundaries in SARS-CoV-2 S-protein amino acid numbering are quoted in brackets. (**D**) Geographical distribution of the eight SARSr-CoV strains, from which S-trimers are studied.

previous structural study on double proline-stabilized BANAL-20-52 and BANAL-20-236 S-trimers under low pH identified both as adopting the locked-2 conformation, with no fatty acid bound to their RBDs (*59*). In line with a previous study (*60*), no contraction of the fatty acid binding pocket, characterized the movement of the "gating helix" (*61*), was observed in the studied SARSr-CoV S-trimers lacking bound fatty acids (fig. S7). Biliverdin has been identified as another small molecule that binds the SARS-CoV-2 S-protein in the NTD, potentially modulating immune responses, including dampening antibody binding toward the SARS-CoV-2 S-protein (*62*, *63*). Among the eight determined SARSr-CoV S-trimer structures, NTD structures, NTD loop structures in particular, vary substantially. Nevertheless, densities compatible with biliverdins have been identified in the NTDs of BANAL-20-52, BtKY72, and YN2013 S-trimers (figs. S8, C, E, and G, and S9).

Variation of SARSr-CoV RBD structures

Among SARSr-CoV S-proteins, the S1 portion, which contains both NTD and RBD, displays substantial sequence variation (figs. S8B and S10B), whereas the S2 portion is relatively conserved. The

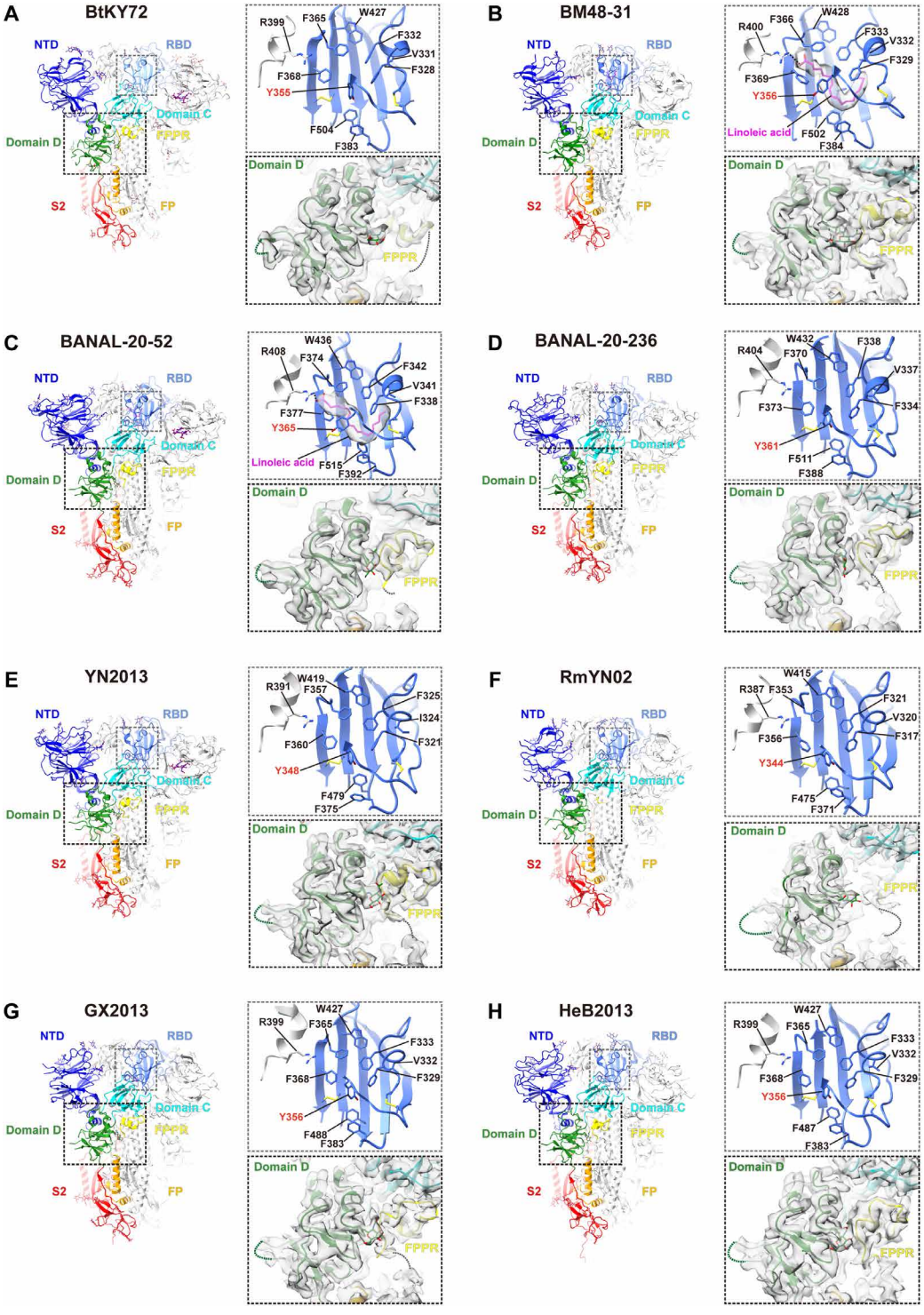

Fig. 2. Structural features of the eight SARSr-CoV S-trimer structures. (**A** to **H**) Structures of BtKY72, BM48-31, BANAL-20-52, BANAL-20-236, YN2013, RmYN02, GX2013, and HeB2013 SARSr-CoV S-trimers are shown in cartoon representations. In each S-trimer, one featured protomer is colored according to the defined domain or functional regions (see Fig. 1C and table S13). The lipid-binding pockets are shown in the gray dashed boxes. Hydrophobic amino acid side chains forming the lipid-binding pocket are shown in stick representations. Modeled LAs (magenta sticks) and their densities in BM48-31 (B) and BANAL-20-52 (C) RBDs are shown. Salt bridge interactions mediated by LAs to arginines of neighboring protomers in BM48-31 (B) and BANAL-20-52 (C) are shown as gray dashed lines. The conserved tyrosines (highlighted by red labels) display a change in side-chain orientation between occupied and empty lipid-binding pockets. In empty lipid-binding pockets, rendering the pockets incompatible with lipid binding. In the black dashed boxes, cryo-EM densities of Domain D and the surrounding regions are shown with fitted molecular models. Among the S-trimer structures, the FPPR in RmYN02 is disordered.

SARSr-CoV RBD is composed of a core domain and an extended loop domain. The RBD core domain is primarily formed by five antiparallel strands (β1 to β4 and β7) and stabilized by three disulfide bonds. BANAL-20-52, BANAL-20-236, BtKY72, BM48-31, YN2013, RmYN02, GX2013, and HeB2013 RBDs essentially share the same core domain structure as the SARS-CoV-2 RBD (Fig. 3, B to D).

The extended loop domain is attached to the exterior of the core domain (Fig. 3, A to D). SARSr-CoV RBDs differ substantially in their extended loop domains, leading to the classification of the eight SARSr-CoV RBDs into three types (fig. S10A). Type-1 includes BANAL-20-52 and BANAL-20-236. The two RBDs have full-length extended loop domains. The SARS-CoV and SARS-CoV-2 RBDs can also be classified as type-1. The extended loop domains of type-1 RBDs feature a concaved outer surface (Fig. 3A). In the middle of the concave, a "lamella" (LM), formed by β5 and β6, is located. On one side of the concave, a disulfide bond–stabilized "large loop" (LL) is located to form a ridge. On the other side of the concave, two smaller loops are positioned. Of these two loops, the loop C-terminal to β6 is called an "anchor loop" (AL), whereas the loop N-terminal to β5 is called a "small loop" (SL). In the SARS-CoV- and SARS-CoV-2-RBD:ACE2 complexes, the "LM," "LL," "AL," and "SL" form contacts to ACE2 (Fig. 3, A to D); therefore, the extended loop domain is also called the RBM. Type-2 includes BM48-31 and BtKY72. In type-2 RBDs, the "SL" within the extended loop domain is deleted. The SL deletion can be either two (BtKY72) or four (BM48-31) amino acids. Type-3 includes YN2013, HeB2013, GX2013, and RmYN02. Among type-3 RBDs, both the "SL" and the disulfide bond–stabilized "LL" are deleted (fig. S10B). Of note, a cross-reactive antibody (SA55) has been found to bind type-1 and type-2 RBDs but not type-3 RBDs (*64*, *65*). A structure comparison of the SA55 epitope on different types of RBDs suggests that a structural change in the AL of type-3 RBDs likely disrupts SA55 binding (fig. S11, B and C).

RBD-RBD interface variations among SARSr-CoV S-trimers

Because of the RBD structure and sequence variations (fig. S10B), the RBD-RBD interfaces within the S-trimer structures show notable differences (Fig. 3, E to H). Compared to SARS-CoV-2 (Fig. 3L), in type-1 BANAL-20-52 S-trimer structures, residues in the RBM LM are highly conserved (conserved $Q493_{SARS2}$ and $Y453_{SARS2}$ are highlighted to show their interaction with the $N370_{SARS2}$ glycan) (Fig. 3I). In type-2 RBDs, basic amino acids can be frequently identified at 493_{SARS2} position in the LM region (fig. S10E). $K482_{BT}$ (BT subscript stands for BtKY72 S-protein numbering), which is equivalent to residue $Q493_{SARS2}$. In another type-2 BM48-31-RBD, $R443_{BM}$ (BM subscript stands for BM48-31 S-protein numbering) is found on the C-terminal side of β5 and buried in the RBD-RBD interface (Fig. 3J and fig. S12C). In type-3 S-trimer structures, the RBD-RBD interface changes drastically with the deletion of the LL. The two strands (β5 and β6) are more polar; therefore, less aromatic residues are found at the interface (Fig. 3K and fig. S12, D to F). Most of the variable residues at or around the RBD-RBD interface are also found to change in the SARS-CoV-2 RBD through antigenic evolution, including 346_{SARS2}, 445_{SARS2}, 452_{SARS2}, 484_{SARS2}, 486_{SARS2}, 490_{SARS2}, 493_{SARS2}, 498_{SARS2}, and 501_{SARS2}. These positions have been proposed to be under a strong immune selection (*62*, *66*–*69*). Several population antibodies have been identified to target 346_{SARS2} (*70*) and 444_{SARS2} (*70*, *71*), 452_{SARS2} and 490_{SARS2} (*72*, *73*), 484_{SARS2} (*74*, *75*), and 501_{SARS2} (*74*, *76*) (Fig. 3L).

Sequence analysis reveals that all the SARSr-CoV S-proteins studied share a common N-glycosylation site at $N370_{SARS2}$ located near the RBD-RBD interface (Fig. 3, I to K, and figs. S10D and S12, A to F). Previous research identified that this glycosylation can affect receptor binding (*77*, *78*), S-trimer conformation (*79*, *80*), antigenicity (*81*), fusogenic activity, and pseudovirus infectivity (*77*, *82*). In type-2 BtKY72 and BM48-31 S-trimers, insertions occur at the N370 glycosylation sequon; however, the sequon is maintained (fig. S10C) and the glycosylation site is preserved (Fig. 3J and fig. S12C).

hACE2 and bat ACE2 binding by the SARSr-CoV S-proteins

We further evaluated our selected SARSr-CoV S-proteins to bind hACE2 using a biolayer interferometry (BLI) assay (fig. S13, J to R, and table S3). hACE2 binding could only be detected for monomeric BANAL-20-52 and BANAL-20-236 RBDs, with dissociation constant (K_D) values of 18 and 27 nM, respectively (fig. S13, C and D, and table S3). These affinities are comparable to that determined for SARS-CoV-2-RBD-monomer (26 nM) (fig. S13I and table S3), consistent with a previous study (*40*). Likely due to the avidity effect, BANAL-20-52 and BANAL-20-236 S-trimers show increased non-dissociating hACE2 binding with K_D values up to 0.009 and 0.79 nM, respectively (fig. S13, L and M, and table S3). The other SARSr-CoV S-trimers show no sign of hACE2 binding (fig. S13, J to K, and N to Q). In addition, in a cell-cell fusion assay mediated by hACE2 as the receptor (*83*), we further found that the abilities of SARSr-CoV S-trimers to induce membrane fusion are largely correlated with their hACE2 binding capabilities. Specifically, only effector cells expressing BANAL-20-236 or BANAL-20-52 S-proteins have been found to fuse with hACE2 expressing target cells (fig. S15, C and D).

We further tested binding of $bACE2_{Ra5538}$ (bat ACE2 of *R. affinis* sample ID 5538) using SARSr-CoV RBDs and S-trimers (fig. S14 and table S4). We found that monomeric BANAL-20-52 and BANAL-20-236 RBDs bind $bACE2_{Ra5538}$ with K_D values of 688 and 104 nM, respectively (fig. S14, C and D). For comparison SARS-CoV-2 RBD binds $bACE2_{Ra5538}$ with a K_D of 705 nM (fig. S14I). Consistently, BANAL-20-52 and BANAL-20-236 S-trimers show avidity-enhanced $bACE2_{Ra5538}$ binding with K_D values in the upper bounds of 0.013 and 1.44 nM, respectively (fig. S14, L and M, and table S4).

We identified that, among SARSr-CoV S-proteins that do not bind hACE2, monomeric BtKY72-RBD binds $bACE2_{Ra5538}$ weakly with a K_D of 3348 nM (fig. S14A). However, BtKY72 S-trimer shows avidity-enhanced $bACE2_{Ra5538}$ binding (K_D in the upper bound of 0.22 nM) (fig. S14J). Consistently, cells expressing BtKY72 S-protein, along with cells expressing BANAL-20-52, BANAL-20-236, and SARS-CoV-2 S-proteins, show abilities to fuse with cells expressing $bACE2_{Ra5538}$ (fig. S15, B to D and F). Therefore, ACE2 binding and cell-cell fusion assays establish that BtKY72 S-protein is able to bind bACE2 selectively over hACE2 (figs. S13J, S14J, and S15F), consistent with a previous report (*84*).

Cryo-EM structure of the BtKY72-RBD-$bACE2_{Ra9479}$ complex

Monomeric BtKY72-RBD, dimeric BtKY72-RBD-Fc, and trimeric BtKY72-S-trimer bind $bACE2_{Ra5538}$ with estimated apparent affinities of 3348, 811, and 0.22 nM, respectively (fig. S16, A to C, and table S5), demonstrating avidity-enhanced binding. Consistent with a previous report (*84*), we further measured that BtKY72-RBD, BtKY72-RBD-Fc, and BtKY72-S-trimer bind $bACE2_{Ra9479}$ (bat

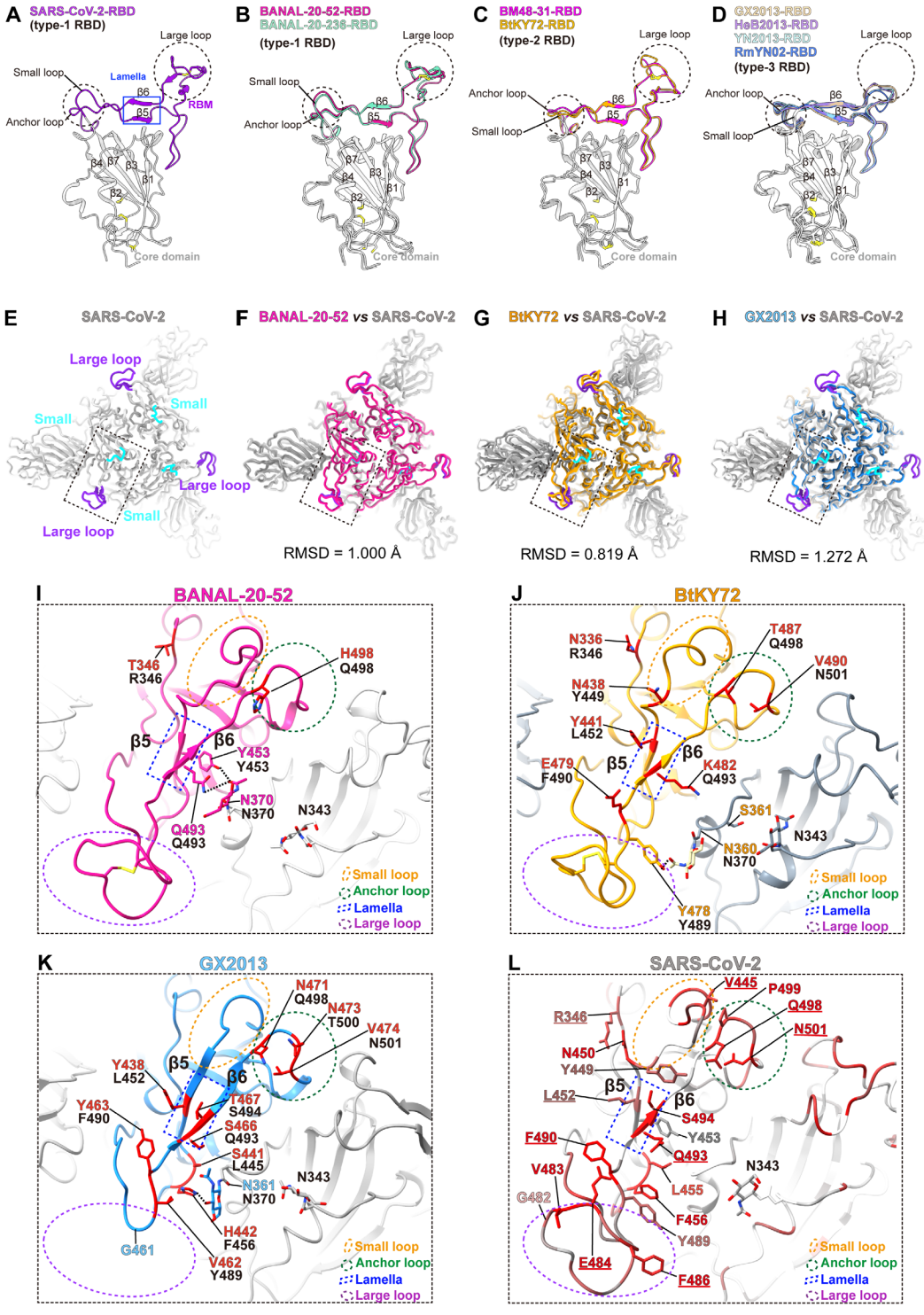

Fig. 3. Structural features of RBDs and RBD-RBD interfaces of selected SARSr-CoV S-trimers. (**A** to **D**) RBD regions of selected SARSr-CoVs are depicted in the same view. The RBMs are highlighted in colors, and the conserved RBD core domains are colored in gray. Dashed circles are shown to mark the locations of the SL, AL, and LL to highlight structural differences in the RBMs of different types of RBDs. (**E**) Top view of SARS-CoV-2 S-trimer in "locked-2" conformation (PDB: 7XU2). LL and SL are highlighted in purple and cyan, respectively. (**F** to **H**) Comparison of type-1 BANAL-20-52, type-2 BtKY72, and type-3 GX2013 S-trimer structures with SARS-CoV-2 to reveal RBD structural differences. The BANAL-20-52 RBDs are colored magenta, BtKY72 RBDs are colored orange, GX0213 RBDs are colored blue, and SARS-CoV-2 RBDs are colored gray as in (E). (**I** to **L**) Zoomed-in views of BANAL-20-52, BtKY72, GX2013, and SARS-CoV-2 RBDs corresponding to the regions within the dashed boxes in (E) to (H). N370 glycan from a neighboring protomer and N370 glycan interacting residues are shown for each S-trimer. Varied residues compared to SARS-CoV-2 are shown as sticks in red. Residues are labeled in their native sequence numbering (colored) and the SARS-CoV-2 numbering (black). (L) The least to most conserved residues among SARSr-CoVs are colored red to white and shown in stick representations at the RBD-RBD interface region in SARS-CoV-2. Among these residues, highly variable positions identified in the antigenic evolution of SARS-CoV-2 are underlined.

ACE2 of *R. affinis* sample ID 9479) with tighter apparent affinities of 144, 105, and 0.12 nM, respectively (fig. S16, D to F, and table S5).

Guided by the binding assays, we obtained the BtKY72-RBD:$bACE2_{Ra9479}$ complex formed between dimeric BtKY72-RBD-Fc and dimeric His-tagged $bACE2_{Ra9479}$. We further determined a cryo-EM structure of the BtKY72-RBD:$bACE2_{Ra9479}$ complex (Fig. 4A and fig. S3, C and F).

In the BtKY72-RBD:$bACE2_{Ra9479}$ complex structure, two bACE2 molecules associate to form a dimeric structure. The $bACE2_{Ra9479}$ is 81% identical to hACE2 in amino acid composition, resulting in an overall structure similar to hACE2 (*85*). The $bACE2_{Ra9479}$ homodimer shares highly conserved dimer interfaces at the C-terminal collectrin-like domain (CLD) neck and peptidase domain (PD) loop regions (Fig. 4A), similar to those observed in the hACE2 homodimer structure (PDB: 6m17) (*86*).

Comparison reveals that BtKY72-RBD:$bACE2_{Ra9479}$ and SARS-CoV-2-RBD:hACE2 complexes are similar in overall structure with a Cα atom RMSD of 0.654 Å (Fig. 4C). In the complex structure of BtKY72-RBD:$bACE2_{Ra9479}$, the total buried surface area (BSA) is 1631.9 $Å^2$ with 840.7 and 791.2 $Å^2$ on RBD and $bACE2_{Ra9479}$, respectively. Two related sarbecovirus RBD complexes formed with different bACE2 molecules were recently reported: PRD-0038-RBD:$bACE2_{Ralc}$ (*Rhinolophus alcyone* ACE2) complex (*60*) has a total BSA of 1542.1 $Å^2$ with 784.9 $Å^2$ on the RBD and 757.2 $Å^2$ on the bACE2. BtKY72-RBD:$bACE2_{Rland}$ (*Rhinolophus lander's horseshoe* bat ACE2) complex (*87*) has a total BSA of 1547.6 $Å^2$ with 802.8 $Å^2$ on the RBD and 744.8 $Å^2$ on the bACE2. Notably, whereas PRD-0038-RBD and BtKY72-RBD have highly similar RBM sequences, $bACE2_{Ra9479}$ differs from both $bACE2_{Ralc}$ and $bACE2_{Rland}$ by several residues at the RBD-ACE2 interaction interface (fig. S17). The BSAs in the BtKY72-RBD:$bACE2_{Ra9479}$ complex is smaller compared to those in the SARS-CoV-2-RBD:hACE2 (PDB:6M0J; total: 1686.7 $Å^2$, SARS-CoV-2-RBD: 864.2 $Å^2$, hACE2: 822.5 $Å^2$) and SARS-CoV-RBD:hACE2 (PDB, 2AJF; total: 1659.5 $Å^2$, SARS-CoV-RBD: 844.1 $Å^2$, hACE2: 815.4 $Å^2$) complexes.

The interface between BtKY72 RBD and $bACE2_{Ra9479}$ contains five hydrogen bonds and one salt bridge, namely, $T489_{BT}$-$Tyr41_{bACE2}$, $Y494_{BT}$-$Glu37_{bACE2}$, $G485_{BT}$-$Lys353_{bACE2}$, $K482_{BT}$-$Asn31_{bACE2}$, $Y478_{BT}$-$Tyr83_{bACE2}$, and $K482_{BT}$-$Glu35_{bACE2}$ (RBD residues are in single-letter abbreviations and ACE2 residues are in three-letter abbreviations) (Fig. 4B, zoomed-in view). By comparison, the interface between wild-type (WT) SARS-CoV-2 RBD and hACE2 has 13 hydrogen bonds and two salt bridges, whereas the SARS-CoV-RBD:hACE2 interface has 13 hydrogen bonds and three salt bridges (fig. S17, C and D, and table S2).

Distinct BtKY72-RBD:$bACE2_{Ra9479}$ interfaces from hACE2 complexes

In the SARS-CoV-2-RBD:hACE2 complex, structural motifs including the LL (amino acids 474 to 490), the LM (formed by β5 and β6 strands), the SL (amino acids 443 to 449), and the AL (amino acids 498 to 505) (Fig. 4, E, H, K, and N, and fig. S17C) are extensively involved in hACE2 binding. Interactions involving these RBM structural elements are notably different in the BtKY72-RBD:$bACE2_{Ra9479}$ complex by comparison with the other hACE2 complexes.

In the BtKY72-RBD:$bACE2_{Ra9479}$ structure, Y478 of the BtKY72-RBD LL forms a hydrogen bond with Tyr83 of $bACE2_{Ra9479}$ (Fig. 4D). The above Y-Tyr interaction is conserved in both SARS-CoV-2- and SARS-CoV-RBD:hACE2 complexes (Fig. 4, E and F). However, distinctively, BtKY72 RBD residue 476 is a glycine ($G476_{BT}$) (Fig. 4D) instead of asparagine ($N473_{SARS1}$ and $N487_{SARS2}$) in both SARS-CoV and SARS-CoV-2 RBDs (Fig. 4, E and F). In addition, in $bACE2_{Ra9479}$, the $Gln24_{hACE2}$ is changed to an arginine ($Arg24_{bACE2}$) (Fig. 4D). The hydrogen bonds formed by SARS-CoV and SARS-CoV-2 RBD residues $N473_{SARS1}$ and $N487_{SARS2}$ to hACE2 residue $Gln24_{hACE2}$ are lost in the BtKY72-RBD:$bACE2_{Ra9479}$ complex (Fig. 4, D to F).

In the LM region, interactions notably vary among the BtKY72, SARS-CoV-2, and SARS-CoV structures. In the BtKY72-RBD:$bACE2_{Ra9479}$ complex, $K482_{BT}$ forms one hydrogen bond ($K482_{BT}$-$Asn31_{bACE2}$) and one salt bridge ($K482_{BT}$-$Glu35_{bACE2}$) to $bACE2_{Ra9479}$ (Fig. 4G). In the SARS-CoV-2-RBD:hACE2 structure, $Q493_{SARS2}$, equivalent to $K482_{BT}$ of BtKY72 RBD, forms a hydrogen bond ($Q493_{SARS2}$-$Glu35_{hACE2}$) with hACE2. This hydrogen bond is further stabilized by an intramolecular salt bridge ($Lys31_{hACE2}$-$Glu35_{hACE2}$) within hACE2 (Fig. 4H). Distinctively, in the SARS-CoV-RBD:hACE2 complex, no specific interaction is formed between the SARS-CoV RBD LM region and hACE2, likely due to the shorter $N479_{SARS1}$ side chain compared to the equivalent $Q493_{SARS2}$ in SARS-CoV-2 RBD (Fig. 4I).

The AL (498 to 505 region) has been identified to play a critical role in binding ACE2 of different animal species (*88*–*90*). In the BtKY72-RBD:$bACE2_{Ra9479}$ structure, the RBD residue $Y494_{BT}$ and $bACE2_{Ra9479}$ residues $Lys353_{bACE2}$ and $Tyr41_{bACE2}$ form an interaction network, such that $Lys353_{bACE2}$ is sandwiched in the middle. In addition, two hydrogen bonds ($T489_{BT}$-$Tyr41_{bACE2}$ and $Y494_{BT}$-$Glu37_{bACE2}$) are formed between BtKY72-RBD and $bACE2_{Ra9479}$ (Fig. 4J). Interactions equivalent to the above are found in both SARS-CoV- and SARS-CoV-2 RBD:hACE2 complexes (Fig. 4, K and L). However, various changes in this region are known to greatly affect ACE2 binding. In the SARS-CoV-RBD:hACE2 complex, comparing to the BtKY72-RBD:$bACE2_{Ra9479}$ complex, an extra π-π interaction is also observed between $Y484_{SARS1}$ (Q498 in SARS-CoV-2) and $Tyr41_{hACE2}$ of hACE2, likely enhancing hACE2 binding (Fig. 4L). In various SARS-CoV-2 variants, the $N501Y_{SARS2}$ substitution has been found to confer mouse ACE2 binding (*90*).

The deletion of two amino acids within the BtKY72-RBD SL prevents small loop:ACE2 interaction in the BtKY72-RBD:$bACE2_{Ra9479}$ complex (Fig. 4M). By contrast, in the SARS-CoV-2-RBD:hACE2 structure, SL residue $Y449_{SARS2}$ engages two hydrogen bonds with $Gln42_{hACE2}$ and $Asp38_{hACE2}$ of hACE2 (Fig. 4N). Similarly, in the SARS-CoV-RBD:hACE2 structure, equivalent hydrogen bonds ($Y436_{SARS1}$-$Gln42_{hACE2}$ and $Y436_{SARS1}$-$Asp38_{hACE2}$) are also formed (Fig. 4O).

Consistently, ACE2 footprint analysis also identifies that BtKY72-RBD lacks ACE2 interactions equivalent to those observed for SARS-CoV-2-RBD residues $N487_{SARS2}$ of LL (Fig. 4, D and E, and fig. S18) and $G447_{SARS2}$ and $Y449_{SARS2}$ of SL (Fig. 4, M and N, and fig. S18E). The analysis further identifies that the hydrophobic interactions mediated by the SARS-CoV-2 RBD residues $F486_{SARS2}$ and $F490_{SARS2}$ are absent in the BtKY72-RBD:$bACE2_{Ra9479}$ complex due to the equivalent residues substituted into L ($L475_{BT}$) and E ($E479_{BT}$), respectively, in BtKY72 RBD (fig. S18, D and E). Last, the salt bridge interaction ($K417_{SARS2}$-$Asp30_{hACE2/bACE2}$) to $Asp30_{hACE2/bACE2}$, mediated by SARS-CoV-2-RBD core domain residue $K417_{SARS2}$, located outside of the four RBM regions, is missing

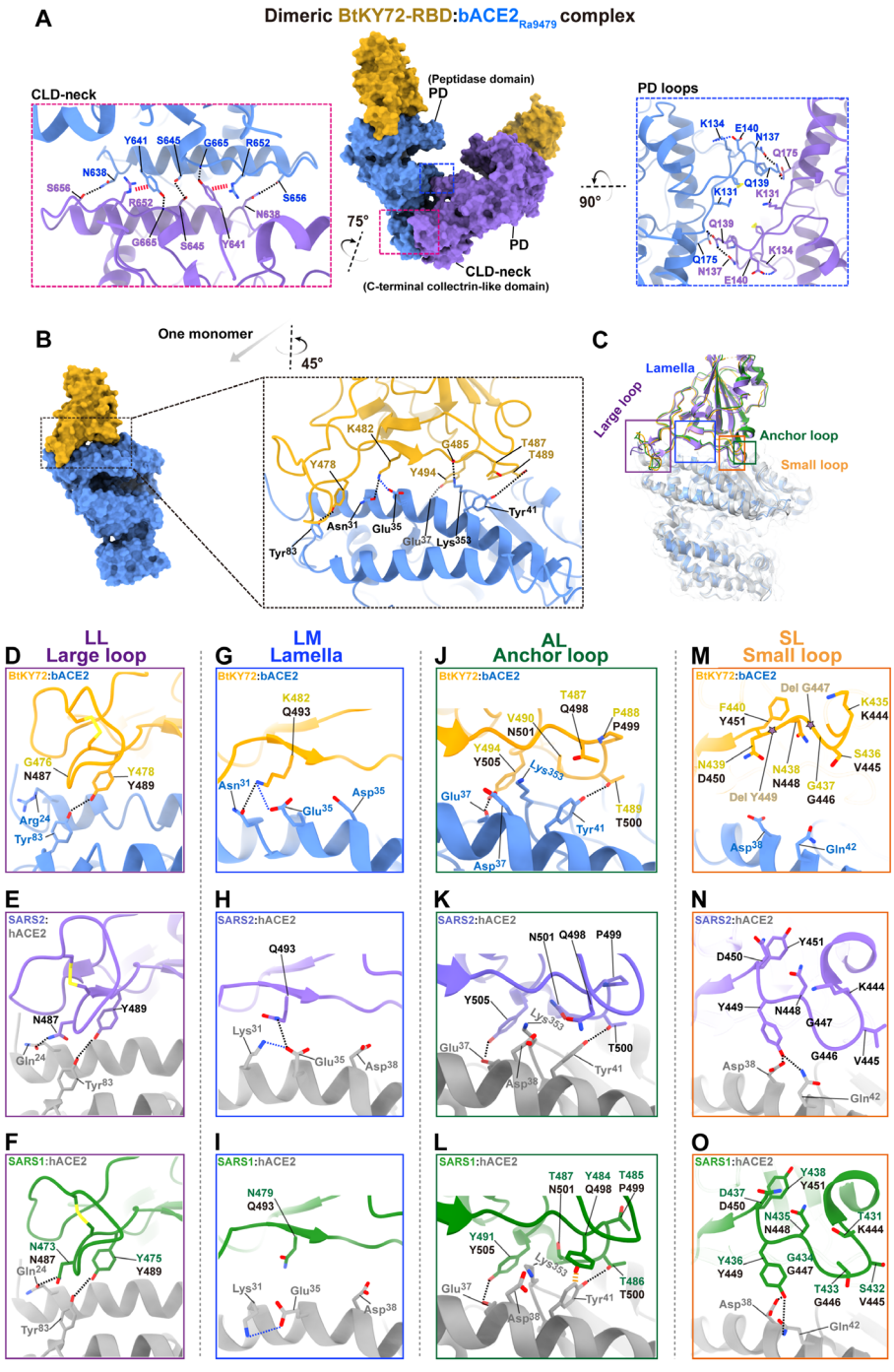

Fig. 4. Cryo-EM structure of the BtKY72-RBD:bACE2$_{Ra9479}$ complex and interaction interface differences among BtKY72-RBD:bACE2$_{Ra9479}$, SARS-CoV-2-RBD:hACE2, and SARS-CoV-RBD:hACE2 complexes. (**A**) Overall structure of the dimeric BtKY72-RBD:bACE2$_{Ra9479}$ complex. Dashed boxes show detailed rotated views of the bACE2$_{Ra9479}$ dimer interfaces in the CLD neck region (left) and the PD loop region (right). Hydrogen bonds are shown as black dashed lines, salt bridges are shown as blue dashed lines, cation-π interactions are shown as red dashed lines and π-π interactions are shown as orange dashed lines. Dashed boxes with corresponding colors in the middle panel indicate locations of the interfaces. (**B**) Left: Structure of a monomeric BtKY72-RBD:bACE2$_{Ra9479}$ complex extracted from the dimeric BtKY72-RBD:bACE2$_{Ra9479}$ complex structure shown in (A). Right: Detailed interactions in the BtKY72-RBD:bACE2$_{Ra9479}$ interface. (**C**) Alignment of BtKY72-RBD:bACE2$_{Ra9479}$, SARS-CoV-2-RBD:hACE2, and SARS-CoV-RBD:hACE2 structures. The interface areas between the RBD external domains and ACE2s in these structures are divided into four regions: LL (purple box), LM (blue box), AL (green box), and SL (orange box). (**D** to **F**) Interactions identified among the BtKY72-RBD:bACE2$_{Ra9479}$ (BtKY72), SARS-CoV-2-RBD:hACE2 (SARS2), and SARS-CoV-RBD:hACE2 (SARS1) structures within the LL region. (**G** to **I**) Interactions identified among the ACE2 complex structures within the LM region. (**J** to **L**) Interactions identified among the ACE2 complex structures within the AL region. (**M** to **O**) Interactions identified among the ACE2 complex structures within the SL region. In the BtKY72:bACE2$_{Ra9479}$ complex, residues equivalent to G447$_{SARS2}$ and Y449$_{SARS2}$ are deleted in the BtKY72-RBD SL, and their locations are marked by stars. [(D) to (O)] Residues are labeled in their native sequence numbering (colored) and the SARS-CoV-2 numbering (black).

in the BtKY72-RBD:bACE2$_{Ra9479}$ complex because the equivalent BtKY72 RBD residue has been substituted to V (V408$_{BT}$) (compare fig. S17A and fig. S17C). Notably, the above extra interactions mediated by SARS-CoV-2 RBD likely contribute to its high-affinity hACE2 binding.

BtKY72 S-protein requiring multiple RBM changes for high-affinity hACE2 binding

We mutated BtKY72 RBD residues to understand how BtKY72 RBD binds selectively to bACE2 over hACE2. A series of dimeric BtKY72-RBD-Fc mutant proteins were generated to allow accurate measurement of weak ACE2 binding by some of these mutants in the BLI assay (Fig. 5 and fig. S19), owing to their enhanced ACE2 binding resulting from the avidity effect (fig. S16 and table S5).

For clarity, each introduced mutation is assigned a specific name based on its location: G476N$_{BT}$ (N487$_{SARS2}$) at the large loop is designated as LL, K482Q$_{BT}$ (Q493$_{SARS2}$) in the lamella as LM, T487Y$_{BT}$ (Y484$_{SARS1}$) at the anchor loop as AL, and last, the reversion of the two–amino acid deletion with a glycine-tyrosine (GY) sequence at the small loop is designated as SL (Fig. 4, M to O). These introduced RBD mutations were designed based on ACE2 interacting amino acids found on equivalent positions of SARS-CoV-2 or SARS-CoV RBDs. In addition, K482Y$_{BT}$ (Q493$_{SARS2}$) and T487W$_{BT}$ (Q498$_{SARS2}$) mutations, previously reported to confer BtKY72 S-protein with the ability to bind hACE2 (*84*), were designated respectively as LM$_Y$ and AL$_W$ and tested for comparison (fig. S19 and table S8).

We found that, although mutated dimeric BtKY72-RBD-Fc proteins with single mutations display either no hACE2 binding or hACE2 binding too weak to be measured by the BLI assay (Fig. 5, A to E, the first row of LL, LM, AL, and SL panels; and table S6), some enhancement of cell fusion was observed in the cell-cell fusion assays mediated by the BtKY72 S-proteins carrying corresponding mutated RBDs (Fig. 5, A to E, the third row), using hACE2 expressing target cells. These results suggest that the cell fusion assay is more sensitive to receptor binding changes (Fig. 5, B to E). For comparison, previously reported LM$_Y$ and AL$_W$ single mutants only conferred very weak hACE2 binding (fig. S19, B and C).

Substantially enhanced hACE2 binding with fast-on, fast-off binding kinetics was observed for BtKY72-RBDs with two simultaneous mutations using the BLI assay (Fig. 5, F, H, and I, the first row of LL+LM, LM+A, and LL+AL panels; and table S6). These BtKY72-RBD-Fc mutants bind hACE2 with apparent K_D values in the range of 83 to 708 nM. Accordingly, obvious increases in cell fusion activity were observed for BtKY72 S-protein mutants carrying two simultaneous RBM mutations, such as LL+LM (Fig. 5F, the third row), LM+AL (Fig. 5H, the third row), and LL+AL (Fig. 5I, the third row) double mutants. This likely correlates with their gradual acquisition of somewhat enhanced, yet weak to intermediate, affinities for hACE2 binding. Consistent with a previous study, LM$_Y$+AL$_W$ (K482Y$_{BT}$ + T487W$_{BT}$) double mutant demonstrated enhanced hACE2 binding (K_D = 86 nM, with fast-on, fast-off kinetics) and cell-cell fusion activities, similar to our LM+AL double mutant (K482Q$_{BT}$ + T487Y$_{BT}$), which also exhibits intermediate hACE2 affinity (K_D = 83 nM) (Fig. 5H, fig. S19D, tables S6 and S8).

Notably, we observed further enhancement of hACE2 binding for triple and quadruple mutants. LL+AL+SL and LL+LM+AL triple mutants show further 29- to 71-fold enhanced binding to hACE2 compared with LL+AL, reaching affinities in the region of 10 to 25 nM (Fig. 5, J and K, and table S6). The quadruple LL+LM+AL+SL mutant exhibits a 3.8 nM affinity to hACE2, representing an increase of 186-fold from the LL+AL double mutant (Fig. 5, L and I, and table S6). The hACE2 affinity achieved by the LL+LM+AL+SL quadruple mutant is nearly equivalent to SARS-CoV-2 (K_D = 1.9 nM; fig. S16H and table S5) and stronger than SARS-CoV (K_D = 7.4 nM; fig. S16K and table S5) RBD-Fc-dimers. Consistent with increased affinities, strong membrane fusion activities were observed for S-proteins carrying the corresponding triple and quadruple RBD mutations.

BtKY72-RBD-Fc carrying the LM mutation has completely lost bACE2 binding in the BLI assay with greatly reduced fusion activity in the cell fusion assay (compare Fig. 5A and Fig. 5C, the second and fourth rows). Conversely, BtKY72-RBD-Fc single LL, AL, or SL mutants demonstrate varying degrees of enhanced bACE2$_{Ra9479}$ binding and fusion activities (Fig. 5, A, B, D, and E). In addition, double or triple BtKY72-RBD-Fc LL+LM, LM+AL, and LL+LM+AL mutants, respectively, are unable to bind bACE2$_{Ra9479}$, indicating that the LM (K482Q$_{BT}$) mutation has a detrimental effect on bACE2 binding (Fig. 5, F, H, and K, and table S7). Dimeric BtKY72-RBD-Fc with LL+AL or LL+AL+SL mutation exhibits substantial 22- or 30-fold enhancement in binding affinity to bACE2$_{Ra9479}$ compared with WT BtKY72-RBD-Fc (Fig. 5, A, I, and J, and table S7). However, when the LL+AL+SL triple mutation is combined with the LM mutation, the generated LL+LM+AL+SL quadruple BtKY72-RBD-Fc mutant displays only a 2.4-fold enhanced affinity for bACE2$_{Ra9479}$ compared with WT BtKY72-RBD-Fc (Fig. 5L and table S7), once again illustrating the detrimental effect of the LM mutation on bACE2$_{Ra9479}$ binding.

Multiple RBM changes also conferring hACE2 affinity to BM48-31 S-protein

We further investigated ACE2 binding by another type-2 S-protein (BM48-31). BM48-31-RBD has a deletion of four AA in the RBM SL, including K444$_{SARS2}$, G446$_{SARS2}$, G447$_{SARS2}$, and Y449$_{SARS2}$, as well as a S482$_{SARS2}$ deletion in the LL (fig. S10B). Previously, BM48-31 was identified as unable to bind ACE2 orthologs (*91*, *92*), except for a recent report showing its usage of *R. alcyone* ACE2 to support pseudovirus entry (*93*). The RBD sequence identity between BM48-31 and BtKY72 is 82.8%, with an RMSD value of 0.96 Å between RBD Cα atoms (Fig. 3C).

We applied a similar mutagenesis strategy to BM48-31-RBD to test whether hACE2 binding can be achieved. In the LL, residues N474$_{BM}$ (N487$_{SARS2}$) and Y476$_{BM}$ (Y489$_{SARS2}$) are conserved compared with both SARS-CoV and SARS-CoV-2 (fig. S10B); therefore, no mutation was introduced in LL. We introduced mutations in the LM region [LM: A480Q$_{BM}$ (Q493$_{SARS2}$) and LM$_1$: R443L$_{BM}$ (L455$_{SARS2}$)], the AL region [AL: T485Y$_{BM}$ (Y484$_{SARS1}$), AL$_1$: S487T$_{BM}$ (T500$_{SARS2}$), and AL$_2$: F492Y$_{BM}$ (Y505$_{SARS2}$)], and the SL region [SL: KGGY insertion, SL$_{half1}$: KG insertion, and SL$_{half2}$: GY insertion] (Fig. 6A).

As expected, the LM$_1$+LM+AL+AL$_1$+AL$_2$+SL mutant shows substantial hACE2 binding (Fig. 6C and table S9). We found that the integrity of the SL region is crucial for ACE2 binding; neither LM$_1$+LM+AL+AL$_1$+AL$_2$+SL$_{half1}$ nor LM$_1$+LM+AL+AL$_1$+AL$_2$+SL$_{half2}$ BM48-31-RBD-Fc mutant with incomplete SL showed hACE2 binding (Fig. 6, D and E, and table S9).

Aligning of BM48-31-RBD into the BtKY72-RBD:bACE2$_{Ra9479}$ complex structure suggests that an arginine at the lamella LM$_1$ position, R443$_{BM}$ (L455$_{SARS2}$), is sterically unfavorable for hACE2 and

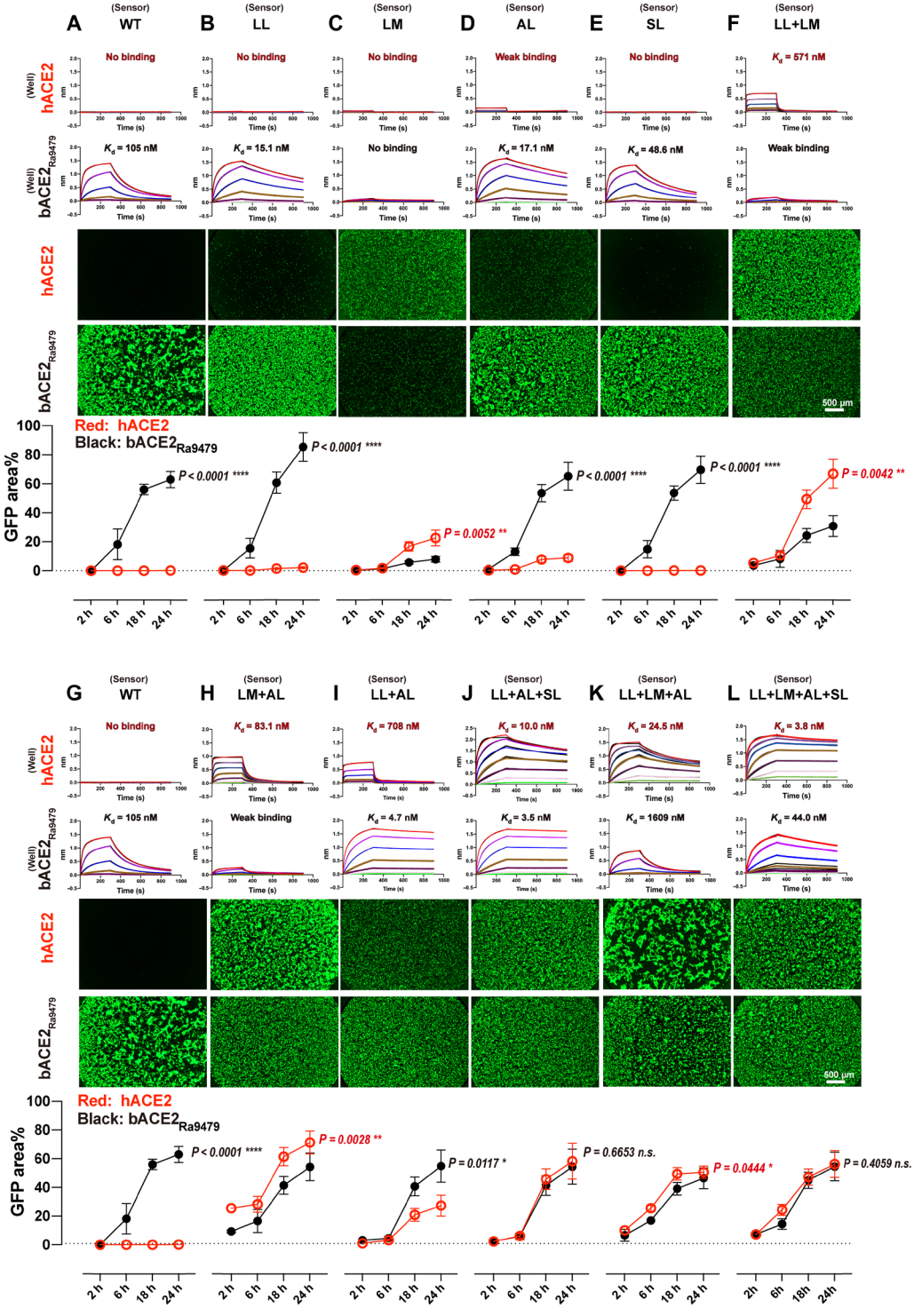

Fig. 5. ACE2 binding and cell-fusion activities of WT and RBM mutant BtKY72 S-proteins. (**A** to **L**) Top two panels: hACE2 and bat ACE2 binding activities as assessed by BLI assays, using dimeric hACE2 or *R. affinis* 9479 bat ACE2 ($bACE2_{Ra9479}$) protein, and measured with different variants of dimeric BtKY72-RBD-Fc protein. BtKY72-RBD-Fc protein variants were immobilized on the sensor tip [indicated by the label "(sensor)" above their names]. hACE2 and bat ACE2 proteins were prepared in wells as threefold serial diluted analyte series, ranging from 3000 to 4.1 nM [denoted by the "(well)" label above their names]. The K_D estimated from each binding experiment is shown alongside with the binding curves. Fitted kinetic parameters are summarized in tables S6 (hACE2) and S7 ($bACE2_{Ra9479}$). Bottom three panels: Cell-cell fusion assays were performed between hACE2 or bACE2 expressing target cells and effector cells expressing WT and variant BtKY72 S-proteins. Fused cells display the GFP signal. Representative images of cell-cell fusion captured at 18 hours posttransfection are shown in the middle two panels. Scale bar, 500 μm. The bottom panels show the quantification of cell-cell fusion measuring the GFP+ area at 2, 6, 18, and 24 hours posttransfection. h, hours.

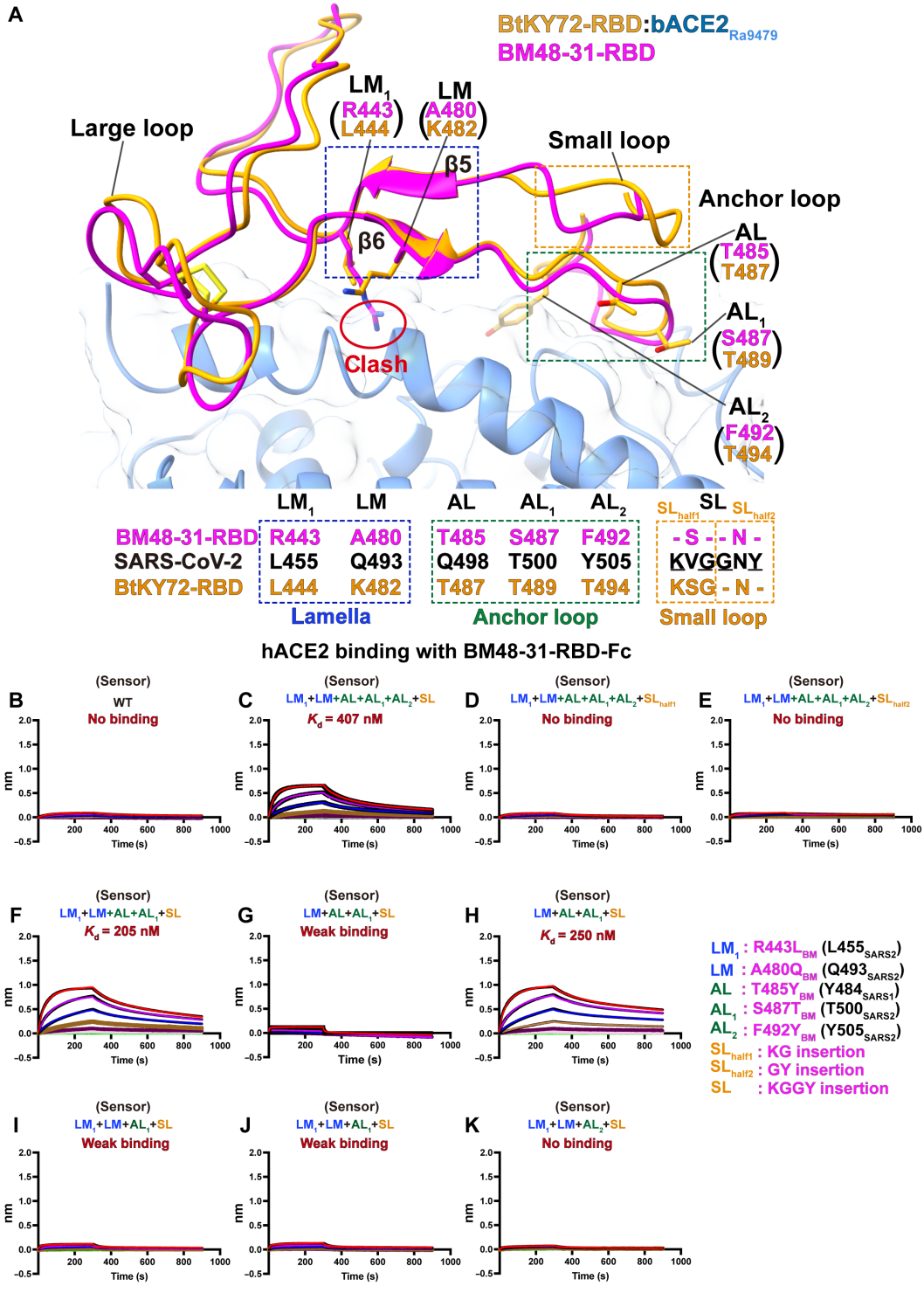

Fig. 6. hACE2 binding activities of WT and RBD mutant BM48-31 S-proteins. (**A**) Top: Structural alignment of BM48-31 RBD into the BtKY72-RBD: bACE2$_{Ra9479}$ complex structure. The different interaction regions are indicated by colored boxes. Bottom: The equivalent amino acids within the ACE2 interface are colored in magenta, black, and orange for BM48-31, SARS-CoV-2, and BtKY72, respectively. BM48-31 RBD variants tested are as follows: LM$_1$: R443L$_{BM}$ (L455$_{SARS2}$), LM: A480Q$_{BM}$ (Q493$_{SARS2}$), AL: T485Y$_{BM}$ (Y484$_{SARS1}$), AL$_1$: S487T$_{BM}$ (T500$_{SARS2}$), AL$_2$: F492Y$_{BM}$ (Y505$_{SARS2}$), SL$_{half1}$: KG insertion, SL$_{half2}$: GY insertion, and SL: KGGY insertion. Equivalent residues in SARS-CoV or SARS-CoV-2 S-protein are shown in black letters. The alignment identifies that R443$_{BM}$ of BM48-31 clashes with bACE2$_{Ra9479}$ binding (red circle). (**B** to **K**) hACE2 binding activities were assessed by BLI assays measuring the interaction between dimeric hACE2 protein and different BM48-31-RBD-Fc variants, including, WT, LM$_1$+LM+AL+AL$_1$+AL$_2$+SL, LM$_1$+LM+AL+AL$_1$+AL$_2$+SL$_{half1}$, LM$_1$+LM+AL+AL$_1$+AL$_2$+SL$_{half2}$, LM$_1$+LM+AL+AL$_1$+SL, LM+AL+AL$_1$+SL, LM$_1$+AL+AL$_1$+SL, LM$_1$+LM+AL$_1$+SL, LM$_1$+LM+AL+SL, and LM$_1$+LM+AL$_2$+SL. BM48-31-RBD-Fc protein variants were immobilized on the sensor tip [indicated by the label "(sensor)" above their names]. The hACE2 protein was prepared into a threefold serial diluted analyte series, ranging from 3000 to 4.1 nM. Fitted kinetic parameters are summarized in table S9.

$bACE2_{Ra9479}$ binding (Fig. 6A and fig. S20). We found that, whereas the LM_1+LM+AL+AL_1+SL (Fig. 6F) mutant shows substantial hACE2 binding, the LM+AL+AL_1+SL mutant fails to bind hACE2 (Fig. 6G). Therefore, we confirm that LM_1 ($R443L_{BM}$) is crucial for hACE2 binding (Fig. 6, F and G).

Last, we identified that the AL ($T485Y_{BM}$) and AL_1 ($S487T_{BM}$) mutations also play crucial roles in hACE2 binding. By comparing with the LM_1+LM+AL+AL_1+SL mutant, omitting the AL or AL_1 mutations, as in the LM_1+LM+AL_1+SL and LM_1+LM+AL+SL mutants, respectively, results in almost no hACE2 binding (Fig. 6, I and J). Furthermore, the LM_1+LM+AL_2+SL mutant, where both the AL+AL_1 mutations were removed from the LM_1+LM+AL+AL_1+AL_2+SL mutant, also shows no hACE2 binding (Fig. 6, C and K). Previous studies have also found that an AL mutation $T487S_{SARS1}$ in civet SARS-CoV viruses (corresponding to $T488_{BM}$ and $N501_{SARS2}$) substantially reduces hACE2 binding (*94*, *95*).

BM48-31-RBD mutants with enhanced hACE2 binding also show substantially increased binding to both $bACE2_{Ra9479}$ and $bACE2_{Ra5538}$ (figs. S21 and S22 and tables S10 and S11).

In cell fusion assays, the WT BM48-31 and LM_1+LM+AL+AL_1+AL_2+SL_{half1} S-proteins showed either no or highly abrogated cell fusion activities, consistent with the absence or substantial reduction in ACE2 binding detected for their RBD-Fc proteins. We found that effector cells expressing LM_1+LM+AL+AL_1+ AL_2+SL, LM_1+LM+AL+AL_1+SL, and LM_1+AL+AL_1+SL mutant S-proteins exhibited substantial capabilities to mediate fusion with target cells expressing hACE2 or $bACE2_{Ra9479}$ (figs. S23, S25, and S26). Such activities were further enhanced in the presence of the protease trypsin (fig. S23). It has recently emerged that a large array of proteases can modulate S-protein mediated cell entry (*96*). We speculate that BtKY72 and BM48-31 S-proteins may differ in protease utilization.

DISCUSSION

In this study, we determined the cryo-EM structures of eight bat SARSr-CoV S-trimers. All eight structures adopt the "locked-2" conformation previously identified as rare conformations for SARS-CoV and SARS-CoV-2 S-trimers (*16*, *25*, *28*, *55*). Among these determined S-trimer structures, fatty acid molecules were found to bind the BM48-31 and BANAL-20-52 S-trimers in their RBDs. Previously, LA binding has been observed in SARS-CoV-2 S-trimers and a few closely related SARSr-CoV S-trimers (*26*). We and others have further confirmed LA binding in the SARS-CoV S-trimer (*16*, *25*). Binding of LA across the RBD:RBD interface has been proposed to stabilize S-trimers in the locked conformation to prevent their premature transition into open or postfusion conformations during virus assembly and egress (*28*). The presence of densities compatible with LAs in the BM48-31 S-trimer, which is distantly related to the SARS-CoV and SARS-CoV-2 S-proteins among SARSr-CoVs, suggests that fatty acid binding may be a widely adopted feature of sarbecovirus S-proteins. However, we were not able to observe LA binding in any S-trimers with type-3 RBDs, despite their LA binding sites remaining intact (Fig. 2, E to H). It is not known whether S-proteins with type-3 RBDs, lacking ACE2 binding activity due to the deletion of both RBM SL and LL loops, require stabilization by the binding of LA. In addition, although biliverdin was not observed in all bat SARSr-CoV S-trimer structures, densities compatible with biliverdins were detected in the BANAL-20-52, BtKY72, and GX2013 S-trimers, carrying type-1, type-2, and type-3 RBDs, respectively. Binding of biliverdin, known to modulate immune response for SARS-CoV-2 (*97*, *98*), to phylogenetically divergent SARSr-CoV S-trimers, suggests that this immune evasion strategy may be widely used within the sarbecovirus subgenus. Cryo-EM only detected locked conformations of SARSr-CoV S-trimers, suggesting that RBD-up conformations may simply be rare. However, the ability of type-1 and type-2 S-trimers to bind ACE2 and mediate cell-cell fusion indicates that they can adopt RBD-up conformations to engage the ACE2 receptor. The stability of the S-trimer is known to influence the distribution of its conformations resolved by cryo-EM (*16*, *56*, *99*). Therefore, it is possible that RBD-up SARSr-CoV S-trimers lacked the stability required to withstand cryo-EM sample preparation, leading to preferential imaging of the more structurally rigid locked S-trimers.

Of note, among the eight SARSr-CoV S-trimers, structures of HeB2013, GX2013, YN2013, and RmYN02 S-trimers, containing type-3 RBDs with both SL and LL deleted, were determined, to our knowledge, for the first time. Both the RBD LL and SL have been identified to play important roles in ACE2 mediated pseudovirus cell entry assays (*100*, *101*). We structurally confirm that the deletion of both loops results in the removal of important ACE2 interacting surfaces, rendering these S-trimers unable to bind ACE2 in the canonical binding mode as observed for both type-1 and type-2 RBDs. Type-3 S-proteins GX2013, YN2013, and HeB2013 were unable to use their cognate ACE2 orthologs for cell entry (fig. S24). A recent study also demonstrates that several type-3 S-proteins are unable to bind a large array of bat ACE2 proteins (*93*).

Our quantitative binding assay, which measures the avidity-enhanced binding between dimeric RBDs and dimeric ACE2 proteins (fig. S16), allowed us to determine that the dimeric BtKY72 RBD-Fc binds to the dimeric $bACE2_{Ra9479}$ with an intermediate-to-weak affinity of 105 nM whereas unable to bind to the dimeric hACE2. Through cryo-EM, we were able to determine the dimeric BtKY72-RBD-Fc:$bACE2_{Ra9479}$ complex. This structure allows us to identify that BtKY72 RBD interacts with bACE2 favorably in the LM region; however, the BtKY72 RBM LM region contains a lysine residue ($K482_{BT}$), making it unfavorable for hACE2 binding. The structure also shows limited interactions to bACE2 by the BtKY72 LL, AL, and SL RBM regions, likely resulting in an intermediate-to-weak bACE2 affinity. To understand how the non-hACE2 binding SARSr-CoV BtKY72 S-protein may acquire high-affinity hACE2 binding, residues known to favor hACE2 binding were introduced in the BtKY72 RBD RBM regions. This approach revealed that while the introduction of individual hACE2-binding-enhancing residues in each RBM region had a weak effect, the simultaneous introduction of multiple residues favoring hACE2 binding across different RBM regions conferred high-affinity hACE2 binding, with an affinity of 3.8 nM—comparable to that of SARS-CoV-2.

Our results indicate that enhanced hACE2 binding generally increases bACE2 affinity as well. We found that both SARS-CoV and SARS-CoV-2 bind bACE2 with relatively high affinities (fig. S16, M to R, and table S5). Introduction of residues favoring hACE2 binding in RBM LL, AL, and SL regions also enhances bACE2 binding. The LL+AL+SL and LL+LM+AL+SL mutants bind both hACE2 and bACE2 with high affinities. Previous studies have proposed that the LM residue ($K482_{BT}$) is key to modulate ACE2 species specificity (*84*, *94*). The high-affinity binding to both hACE2 and bACE2 by

these two mutants suggests that an adverse LM interaction may be overcome, in the presence of other RBM ACE2 binding enhancing residues, to achieve high-affinity ACE2 binding. However, our results also confirm that at low or intermediate ACE2 background affinities, interaction in the LM region can serve as an on-off switch to dictate ACE2 species specificity, as proposed before (*94*). Substituting BtKY72-RBD $K482_{BT}$ ($Q493_{SARS2}$) to alanine (A), asparagine (N), or glutamine (Q) all results in a drastic reduction in binding affinity to $bACE2_{Ra9479}$ (fig. S27 and table S12). A recent study on the BtKY72 S-protein further confirmed that single mutations at $K482_{BT}$ have a differential effect on hACE2 and bACE2 binding (*87*). In Khosta-2, which is closely related to BtKY72, a change of $Q478_{Khosta-2}$ ($Q493_{SARS2}$) to a lysine resulted in a greater than 10-fold reduction in cell entry with hACE2 as the receptor (*102*). In addition, in SARS-CoV, introduction of a lysine or arginine residue in LM has been found to greatly reduce affinity to hACE2 and increase affinity to civet ACE2 (*94*).

Therefore, our results demonstrate that molecular determinants for high-affinity ACE2 binding are distributed across the four ACE2 interacting regions within the sarbecovirus S-protein RBM, namely, the LL, LM, AL, and SL regions, rather than being concentrated at a single specific RBM location. Favorable ACE2 interactions in these regions have a cumulative effect, working synergistically to achieve strong ACE2 binding. In SARS-CoV-2, optimal hACE2 interactions are found in all the four regions. The resulting high-affinity hACE2 binding may allow greater flexibility in RBM antigenic changes while retaining binding to the ACE2 receptor. Such a feature may have allowed the LM region antigenic $Q493R_{SARS2}$ change, with the effect of reducing hACE2 binding, to occur in the SARS-CoV-2 Omicron BA.1/2/3 RBDs (*89*, *103*).

The synergistical effect from different RBM regions can also explain the varied affinities observed for other SARSr-CoV S-proteins. RaTG13 and RshSTT182/200 bind hACE2 with 183- and 888-fold weaker affinity than SARS-CoV-2. RaTG13 RBD differs from SARS-CoV-2 RBD by six amino acids. Of these, four changes ($Y449F_{SARS2}$, $F486L_{SARS2}$, $N501D_{SARS2}$, and $Y505H_{SARS2}$), known to reduce hACE2 binding, are in the LL and AL regions, whereas two changes, favoring hACE2 binding, are found in LM ($Q493Y_{SARS2}$) and AL ($Q498Y_{SARS2}$) regions. The combined effect of these changes in the RaTG13 type-1 RBM likely results in weakened hACE2 binding compared to SARS-CoV-2 (*37*). For RshSTT182/200, encoding a type-2 RBM with the SL deleted, combining the reversion of the SL, a mutation in the LL, and the T346R change, a 125-fold increase in hACE2 binding can be achieved; however, the achieved affinity was still sevenfold lower by comparison with SARS-CoV-2 (*104*).

Similarly, hACE2-binding-enhancing mutations in the RBM also act synergistically to confer intermediate affinities for both hACE2 and bACE2, as well as ACE2-mediated cell fusion activity, to the BM48-31 S-protein. We additionally identified that, in the case of BM48-31, the acquired cell-fusion activities can be substantially enhanced by the presence of the protease trypsin, thereby highlighting the interplay between receptor binding and other entry-promoting factors for SARSr-CoV S-proteins.

While synergistic mutations across different RBM regions enabled the type-2 BtKY72 S-RBD to bind hACE2 with high affinity, a similar approach only conferred intermediate affinity to the type-2 BM48-31 S-RBD, which generally lacks ACE2 binding activity. The weaker hACE2 affinity achieved suggests that amino acid differences outside of the RBM regions may further modulate ACE2 binding affinity (*93*). These observations suggest that there are substantial genetic barriers for SARSr-CoV S-proteins with type-2 and type-3 RBDs, which lack RBM features for optimal hACE2 interaction, to acquire an hACE2 affinity comparable to known human-infecting sarbecoviruses—SARS-CoV and SARS-CoV-2. Although the results also suggest a potentially lower genetic barrier to high-affinity hACE2 binding for S-proteins with type-1 RBDs, optimal interactions in all the RBM regions remain rarely identified among type-1 RBDs. Continued surveillance and testing of ACE2 binding are essential to discover whether an animal reservoir already hosting SARSr-CoVs with strong hACE2 affinity.

MATERIALS AND METHODS

Protein constructs

S genes of BtKY72 (taxonomy ID: 903610), BM48-31 (taxonomy ID: 864596), YN2013 (taxonomy ID: 1503303), RmYN02 [The Global Initiative on Sharing Avian Influenza Data (GISAID): EPI_ISL_412977], GX2013 (taxonomy ID: 1503301), and HeB2013 (Taxonomy ID: 1503296) were codon optimized and synthesized by GenScript (Nanjing, China). S genes of BANAL-20-52 (GISAID: EPI_ISL_4302644) and BANAL-20-236 (GISAID: EPI_ISL_4302647) were synthesized by the Sango Company (Shanghai, China). The transmembrane domains and C-terminal ends of BtKY72 (amino acids 1194 to 1257), BM48-31 (amino acids 1195 to 1259), YN2013 (amino acids 1169 to 1233), GX2013 (amino acids 1178 to 1242), HeB2013 (amino acids 1177 to 1241), RmYN02 (amino acids 1163 to 1227), BANAL-20-52 (amino acids 1205 to 1269), and BANAL-20-236 (amino acids 1201 to 1265) were removed before a T4 trimerization foldon, HRV 3C cleavage site, an Octo-His tag, and a double strep-tag were added to the C termini. Two proline mutations (K946P and V947P) were introduced to stabilize the YN2013 S-protein, as previously described (*105*). All S-protein constructs were cloned into the pCDNA3.1 vector with their native signal peptides to allow secretory expression.

hACE2, *R. affinis* 9479 (sample name: Ra9479, GenBank: QMQ39227) ACE2 ($bACE2_{Ra9479}$), and *R. affinis* 787 (sample name: Ra5538, GenBank: QMQ39222) ACE2 ($bACE2_{Ra5538}$) genes were synthesized. The PD (amino acids 1-615) of the bat *R. affinis* $bACE2_{Ra9479}$, $bACE2_{Ra5538}$, and hACE2 were fused to the Fc domain of human immunoglobulin G (IgG), resulting in $bACE2_{Ra9479}$-Fc, $bACE2_{Ra5538}$-Fc, and hACE2-Fc constructs. In addition, a different version of ACE2 construct, containing the PD and the CLD (amino acids 1 to 731), bearing a C-terminal Hexa-His tag, was generated for hACE2, $bACE2_{Ra9479}$, and $bACE2_{Ra5538}$. All ACE2 constructs were cloned into the pCDNA3.1 vector with their native signal peptides to allow secretory expression. Because of the presence of the CLD, these His-tagged ACE2 proteins form dimers.

BtKY72 RBD and variants (amino acids 309 to 530 residues), BM48-31 RBD and variants (amino acids 310 to 524 residues), BANAL-20-52 RBD (amino acids 330 to 528 residues), BANAL-20-236 RBD (amino acids 326 to 524 residues), YN2013 RBD (amino acids 302 to 501 residues), RmYN02 RBD (amino acids 298 to 497 residues), GX2013 RBD (amino acids 310 to 510 residues), and HeB2013 RBD (amino acids 310 to 509 residues) were fused with C-terminal Hexa-His tags. In addition, RBD-Fc constructs were generated by fusing RBDs with human IgG Fc domains. All RBD constructs were cloned into the pCDNA3.1vector with N-terminal mu-phosphatase signal peptide sequences to allow secretory expression.

Protein expression and purification

Proteins were expressed by transient transfection in Expi293F cells, 1 mg of DNA was transfected into 1 liter of cells using linear polyethylenimine transfection reagent. After transfection, cells were cultured at 33°C for 3.5 to 4.0 days for S-proteins and 5 days for RBD and ACE2 proteins. For His-tagged S-proteins and RBD proteins, the supernatants were harvested by centrifugation and 25 mM phosphate (pH 8.0), 3 mM imidazole, 300 mM NaCl, and 0.5 mM phenylmethylsulfonyl fluoride were supplemented. The supernatant was recirculated for about 2.5 times onto a 5-ml Talon cobalt column, and the column was washed with 100 ml of buffer A [25 mM phosphate (pH 8.0), 5 mM imidazole, and 300 mM NaCl]. Proteins were eluted using a linear gradient with increasing concentration of buffer B [25 mM phosphate (pH 8.0), 500 mM imidazole, and 300 mM NaCl]. Eluted protein samples were quality checked by SDS–polyacrylamide gel electrophoresis, concentrated, and buffer exchanged into phosphate-buffered saline (PBS) using a 100-kDa (for S-proteins) or 10-kDa (for RBD proteins) MWCO Amicon Ultra filtration device (Merck Millipore). The concentrated proteins were frozen in liquid nitrogen and stored at −80°C.

For RBD-Fc and ACE2-Fc proteins, 5 days posttransfection, each culture supernatant was cleared by filtering through a 0.45-μm filter membrane before being loaded onto a 5-ml HiTrap Protein A column (Cytiva). The column was washed with PBS [10 mM Na_2HPO_4 and 1.8 mM KH_2PO_4 (pH 7.4), 137 mM NaCl, and 2.7 mM KCl]. Proteins were eluted using a linear gradient with increasing concentration of a citrate buffer [0.1 M citric acid (pH 3.0)]. Eluted protein fractions were immediately neutralized with equal volumes of 1.0 M tris-HCl (pH 8.0) buffer. RBD-Fc and ACE2-Fc proteins were concentrated and buffer exchanged into PBS before being frozen and stored at −80°C.

BLI binding analysis

Binding of SARSr-CoV S-proteins or RBDs to ACE2-Fc proteins was assessed using BLI on an Octet RED 96 instrument (FortéBio, USA). All steps were performed at 25°C with an orbital shaking speed of 1000 rpm. All reagents were formulated in PBS-TB buffer (PBS with 0.02% v/v Tween 20 and 0.1% (w/v) bovine serum albumin). Before the experiments, all protein A biosensors were pre-equilibrated in the PBS-TB buffer for 10 min. ACE2-Fc proteins (11 μg/ml) were immobilized onto Protein A biosensors (FortéBio, USA) to a response value of ~1.2 nm. After a 60-s baseline step in PBS-TB, the biosensors immobilized with ACE2-Fc proteins were submerged in the analyte (S-proteins or RBDs) solutions for 300 s to measure association, before being submerged in PBS-TB for 600 s to measure dissociation. Data were reference subtracted and analyzed in the FortéBio Data Analysis Software (FortéBio) by fitting to 1:1 or 2:1 binding models to determine k_{on}, k_{off}, and K_D values as previously described (*106*). Raw data and fits were plotted using GraphPad Prism 8 (GraphPad Software). For binding by monomeric RBDs, weak binding is defined as response values between 0.02 and 0.08 nm, with values below 0.02 nm indicating no binding. Binding parameters were not determined from weak binding data.

Binding of dimeric His-tagged hACE2, $bACE2_{Ra5538}$, and $bACE2_{Ra9479}$ to SARSr-CoV RBD-Fc proteins was assessed using the BLI assay. The RBD-Fc proteins (11 μg/ml) were loaded onto Protein A biosensors (FortéBio, USA) to a level of ~1.2 nm. After a 60-s baseline step in PBS-TB buffer, the biosensors immobilized with RBD-Fc proteins were submerged in the ACE2 protein solutions for 300 s to measure association, before being submerged in PBS-TB for 600 s to measure dissociation. Data were reference subtracted and analyzed in the FortéBio Data Analysis Software. For binding by dimeric ACE2 proteins, weak binding is defined as response values between 0.08 and 0.3 nm, with values below 0.08 nm indicating no binding. Binding parameters were not determined from weak binding data.

Cryo-EM grid preparation and data acquisition

Cryo-EM grids were prepared with S-trimer samples at concentrations between 1.2 and 2.5 mg/ml. All grids were prepared by applying 3.0 μl of S-trimer solutions directly to glow discharged (15 mA, 30 s) holey carbon grids (Quantifoil Cu mesh 300 R1.2/R1.3) before blotting, except for GX2013. GX2013 S-trimer samples were supplemented with 0.1% (w/v) octyl glucoside (OG) immediately before being applied to grids, to reduce preferred orientation of particles. Cryo-EM grids were blotted for 2.5 s with a blot force of 4, before being plunge frozen into liquid ethane using a Vitrobot Mark IV (Thermo Fisher Scientific) at 4°C and 100% humidity.

For GX2013 and BANAL-20-236 and RmYN02 S-proteins, cryo-grids were loaded into a Talos Arctica electron microscope (Thermo Fisher Scientific) operated at 200 keV for data collection using the Serial EM software (Mastronarde, 2005). Micrographs were recorded at a nominal magnification of ×45,000 on a K3 direct detection camera (Gatan) with a range of defocus −0.8 to −2.5 μm with a super-resolution counting mode at pixel size of 0.44 Å. The exposure was performed with a dose rate of 25 e^-/pixel per second and an accumulative dose of ~60 $e^-/Å^2$ for each movie, which was fractionated into 27 subframes.

For BtKY72, BM48-31, BANAL-20-52, YN2013, and HeB2013 S-proteins, micrographs were collected using the EPU software (Thermo Fisher Scientific) on a Titan Krios G3i electron microscope (Thermo Fisher Scientific) operated at 300 keV. Micrographs were recorded at a nominal magnification of ×81,000 on a K3 direct electron detector (Gatan) coupled to a Gatan BioQuantum energy filter set with a slit width of 10 eV and with a defocus range between −0.8 and −2.0 μm. Each movie was collected with a dose rate of 25 e^-/pixel per second, fractioned into 38 frames, and exposed for 2.28 s, resulting in a total dose of 50 $e^-/Å^2$ with a calibrated pixel size of 1.095 Å.

The BtKY72-RBD:$bACE2_{Ra9479}$ complex at a concentration of 11 μM was formed by incubating BtKY72-RBD-Fc protein and $bACE2_{Ra9479}$ (amino acids 1 to 731) in equal molar amounts for 2 hours at 4°C. Three microliters of the complex was supplemented with 0.075% (w/v) OG immediately before being applied to glow discharged (15 mA, 30 s) Ni-Au-300 mesh R1.2/1.3 grids. Grids were blotted for 2.5 s with a blot force of 4 before being plunge frozen into liquid ethane using a Vitrobot Mark IV (Thermo Fisher Scientific) at 4°C and 100% humidity. Micrographs were collected on a Titan Krios G4i electron microscope (Thermo Fisher Scientific) operated at 300 keV using the EPU software (Thermo Fisher Scientific). Micrographs were recorded at a nominal magnification of ×165,000 on a Falcon 4 direct electron detector coupled to a Selectris-X imaging filter set with a slit width of 10 eV (Thermo Fisher Scientific) and with a defocus range between −0.8 and −2.4 μm. Each movie was collected with a dose rate of 15 e^-/pixel per second, exposed for

1.78 s, resulting in a total dose of 50 $e^{-}/Å^2$ with a calibrated pixel size of 0.73 Å.

Image processing

Movies were aligned in RELION 3.1 using RELION's own implementation (*107*) of MotionCor2 algorithm (*108*). Contrast transfer function (CTF) estimation and template-free particle picking were performed in Warp (*109*). Particles extracted by Warp were subsequently imported into RELION. For each dataset, an EM structure of the SARS-CoV-2 S-protein in a locked conformation (EMD-11329) (*24*) was filtered to 60-Å resolution to be used as the initial reference in the first round of three-dimensional (3D) classification. The first round of 3D classification was performed at 2× binning to identify S-trimer particles. 3D classes displaying clear secondary structures were pooled and subjected to one round of 2D classification to remove bad particles before a second round of 3D classification. Autorefinement, CTF refinement, and Bayesian polishing were performed for the classified datasets. Following a final round of 3D autorefinement, map resolutions were estimated at the 0.143 criterion of the phase randomization–corrected Fourier shell correlation curve calculated between two independently refined half-maps multiplied by a soft-edged solvent mask. Final reconstructions were sharpened and locally filtered using RELION. Dataset processed by the cryoSPARC package was first particle picked before 2D classification was performed. Well-featured particles from the 2D classification were subjected to ab initio 3D classification. Homogeneous refinement and local refinement were applied to the set of particles with good features identified by the ab initio 3D classification.

For the BtKY72-RBD:$bACE2_{Ra9479}$ complex dataset, data processing was performed mainly using cryoSPARC (*110*). After patch-motion correction and CTF estimation, micrographs with CTF fit resolution above 6 Å were picked by curate exposures job. Then, particles were picked using a blob picker to get templates for the subsequent template picker. Picked particles were extracted at 3x binning and subjected to 2D classification, ab initio reconstruction, and heterogeneous refinement. Particles belonging to classes with high-resolution detail were selected for a final round of Topaz picker by Topaz cross-validation job. Picked particles were extracted at 3x binning and subjected to 2D classification, ab initio reconstruction, and heterogeneous refinement again. Highly similar classes in heterogeneous refinement showing high-resolution detail were combined and reextracted at 1.5x binning and subjected to nonuniform refinement with optimization of per-group CTF parameters. The CTF-refined particles and volumes were subjected to reference-based motion correction and an extra round of nonuniform refinement to get the final dimeric structure.

Because of conformational dynamics in the dimeric structure, several local regions were resolved to lower resolution. Local refinement was applied to improve the local resolution at the binding interface. Particles were symmetry expanded and imported into RELION 4.0, where the dynamic parts were masked and particles were subtracted through masking. The subtracted particles were imported back to cryoSPARC to perform local refinement jobs. Given the fact that higher-order aberrations were lost during particle porting between the two software, multiple global CTF Refinement and local refinement iterations were performed to compensate for this loss before the final local structure map was obtained.

Model building and structure refinement

A previously determined SARS-CoV-2 S-trimer structure (PDB ID: 6ZP2) (*24*) was used as the starting models for the SARSr-CoV S-trimer structures. Model building and adjustment were performed manually in Coot 0.9 (*111*). Steric clash and side-chain rotamer conformations were improved using the Namdinator web server (*112*). Final structures after additional manual adjustments were refined and validated in PHENIX-1.18.261 (*113*). The SARS-CoV-2-RBD:hACE2-B^0AT_1 complex structure (PDB ID: 6M17, EMD-30039) (*86*, *114*) was used as the starting model for the BtKY72-RBD: $bACE2_{Ra9479}$ complex structure. The starting model was fitted in the cryo-EM density in Chimera before manual adjustments were carried out in Coot. The model was refined by multiple rounds of refinement in Namdinator and PHENIX. Data collection and refinement statistics for all the reported structures are provided in table S1.

GFP-split fusion assay

The split–green fluorescent protein (GFP) system–based cell-cell fusion assay mediated by the interaction between S-protein and ACE2 receptor was previously described (*83*). Briefly, human embryonic kidney (HEK) 293T cells transfected with pcDNA3.1 encoding C-terminally FLAG-tagged (DYKDDDDK) full-length S-proteins with native signal peptides and pQCXIP-GFP1-10 were prepared as effector cells, whereas HEK293T cells transfected with hACE2 or bat ACE2 (bACE2, $bACE2_{Ra5538}$, or $bACE2_{Ra9479}$) and pQCXIP-BSR-GFP11 served as the target cells. Twenty-four hours after transfection, effector and target cells were washed and resuspended in Dulbecco's Modified Eagle's Medium (DMEM) containing 10% fetal bovine serum (FBS) without trypsin treatment, mixed at a 1:1 ratio, and plated at ~2×10^5 cells per well in 96-well plate. Fluorescence images were recorded at the indicated time points using a Nikon TS2-S-SM fluorescence microscope. For BM48-31 S-proteins, effector and target cells were digested with 0.25% trypsin-EDTA for 5 min at room temperature, before being washed and mixed in DMEM with 10% FBS to initiate the cell-cell fusion assay. The GFP area was quantified with ImageJ. S-protein expression was analyzed via flow cytometry using a SARS-CoV-2 S2 antibody (1:2500 dilution, Sino Biological, 40590-T62) and Western blot using an anti-FLAG antibody (1:1000 dilution, Sino Biological, 109143-MM13). The GFP area was normalized to the mean fluorescence intensity of surface S-proteins.

Supplementary Materials

This PDF file includes:

Figs. S1 to S27

Tables S1 to S13

REFERENCES AND NOTES

1. R. A. M. Fouchier, T. Kuiken, M. Schutten, G. van Amerongen, G. J. J. van Doornum, B. G. van den Hoogen, M. Peiris, W. Lim, K. Stohr, A. D. M. E. Osterhaus, Aetiology: Koch's postulates fulfilled for SARS virus. *Nature* **423**, 240 (2003).
2. J. S. M. Peiris, C. M. Chu, V. C. C. Cheng, K. S. Chan, I. F. N. Hung, L. L. M. Poon, K. I. Law, B. S. Tang, T. Y. W. Hon, C. S. Chan, K. H. Chan, J. S. C. Ng, B. J. Zheng, W. L. Ng, R. W. M. Lai, Y. Guan, K. Y. Yuen, HKU/UCH SARS Study Group, Clinical progression and viral load in a community outbreak of coronavirus-associated SARS pneumonia: A prospective study. *Lancet* **361**, 1767–1772 (2003).
3. C. Drosten, S. Günther, W. Preiser, S. van der Werf, H.-R. Brodt, S. Becker, H. Rabenau, M. Panning, L. Kolesnikova, R. A. M. Fouchier, A. Berger, A.-M. Burguière, J. Cinatl, M. Eickmann, N. Escriou, K. Grywna, S. Kramme, J.-C. Manuguerra, S. Müller, V. Rickerts,

M. Stürmer, S. Vieth, H.-D. Klenk, A. D. M. E. Osterhaus, H. Schmitz, H. W. Doerr, Identification of a novel coronavirus in patients with severe acute respiratory syndrome. *N. Engl. J. Med.* **348**, 1967–1976 (2003).
4. J. S. M. Peiris, Y. Guan, K. Y. Yuen, Severe acute respiratory syndrome. *Nat. Med.* **10**, S88–S97 (2004).
5. P. Zhou, X.-L. Yang, X.-G. Wang, B. Hu, L. Zhang, W. Zhang, H.-R. Si, Y. Zhu, B. Li, C.-L. Huang, H.-D. Chen, J. Chen, Y. Luo, H. Guo, R.-D. Jiang, M.-Q. Liu, Y. Chen, X.-R. Shen, X. Wang, X.-S. Zheng, K. Zhao, Q.-J. Chen, F. Deng, L.-L. Liu, B. Yan, F.-X. Zhan, Y.-Y. Wang, G.-F. Xiao, Z.-L. Shi, A pneumonia outbreak associated with a new coronavirus of probable bat origin. *Nature* **579**, 270–273 (2020).
6. W.-J. Guan, Z.-Y. Ni, Y. Hu, W.-H. Liang, C.-Q. Ou, J.-X. He, L. Liu, H. Shan, C.-L. Lei, D. S. C. Hui, B. Du, L.-J. Li, G. Zeng, K.-Y. Yuen, R.-C. Chen, C.-L. Tang, T. Wang, P.-Y. Chen, J. Xiang, S.-Y. Li, J.-L. Wang, Z.-J. Liang, Y.-X. Peng, L. Wei, Y. Liu, Y.-H. Hu, P. Peng, J.-M. Wang, J.-Y. Liu, Z. Chen, G. Li, Z.-J. Zheng, S.-Q. Qiu, J. Luo, C.-J. Ye, S.-Y. Zhu, N.-S. Zhong, China Medical Treatment Expert Group for Covid-19, Clinical characteristics of coronavirus disease 2019 in China. *N. Engl. J. Med.* **382**, 1708–1720 (2020).
7. R. Lu, X. Zhao, J. Li, P. Niu, B. Yang, H. Wu, W. Wang, H. Song, B. Huang, N. Zhu, Y. Bi, X. Ma, F. Zhan, L. Wang, T. Hu, H. Zhou, Z. Hu, W. Zhou, L. Zhao, J. Chen, Y. Meng, J. Wang, Y. Lin, J. Yuan, Z. Xie, J. Ma, W. J. Liu, D. Wang, W. Xu, E. C. Holmes, G. F. Gao, G. Wu, W. Chen, W. Shi, W. Tan, Genomic characterisation and epidemiology of 2019 novel coronavirus: Implications for virus origins and receptor binding. *Lancet* **395**, 565–574 (2020).
8. C. Huang, Y. Wang, X. Li, L. Ren, J. Zhao, Y. Hu, L. Zhang, G. Fan, J. Xu, X. Gu, Z. Cheng, T. Yu, J. Xia, Y. Wei, W. Wu, X. Xie, W. Yin, H. Li, M. Liu, Y. Xiao, H. Gao, L. Guo, J. Xie, G. Wang, R. Jiang, Z. Gao, Q. Jin, J. Wang, B. Cao, Clinical features of patients infected with 2019 novel coronavirus in Wuhan, China. *Lancet* **395**, 497–506 (2020).
9. N. Zhu, D. Zhang, W. Wang, X. Li, B. Yang, J. Song, X. Zhao, B. Huang, W. Shi, R. Lu, P. Niu, F. Zhan, X. Ma, D. Wang, W. Xu, G. Wu, G. F. Gao, W. Tan, China Novel Coronavirus Investigating and Research Team, A novel coronavirus from patients with pneumonia in China, 2019. *N. Engl. J. Med.* **382**, 727–733 (2020).
10. W. Li, M. J. Moore, N. Vasilieva, J. Sui, S. K. Wong, M. A. Berne, M. Somasundaran, J. L. Sullivan, K. Luzuriaga, T. C. Greenough, H. Choe, M. Farzan, Angiotensin-converting enzyme 2 is a functional receptor for the SARS coronavirus. *Nature* **426**, 450–454 (2003).
11. S. C. Harrison, Viral membrane fusion. *Nat. Struct. Mol. Biol.* **15**, 690–698 (2008).
12. J. Zhang, T. Xiao, Y. Cai, B. Chen, Structure of SARS-CoV-2 spike protein. *Curr. Opin. Virol.* **50**, 173–182 (2021).
13. B. J. Bosch, R. van der Zee, C. A. de Haan, P. J. M. Rottier, The coronavirus spike protein is a class I virus fusion protein: Structural and functional characterization of the fusion core complex. *J. Virol.* **77**, 8801–8811 (2003).
14. M. Gui, W. Song, H. Zhou, J. Xu, S. Chen, Y. Xiang, X. Wang, Cryo-electron microscopy structures of the SARS-CoV spike glycoprotein reveal a prerequisite conformational state for receptor binding. *Cell Res.* **27**, 119–129 (2017).
15. W. Song, M. Gui, X. Wang, Y. Xiang, Cryo-EM structure of the SARS coronavirus spike glycoprotein in complex with its host cell receptor ACE2. *PLOS Pathog.* **14**, e1007236 (2018).
16. X. Zhang, Z. Li, Y. Zhang, Y. Liu, J. Wang, B. Liu, Q. Chen, Q. Wang, L. Fu, P. Wang, X. Zhong, L. Jin, Q. Yan, L. Chen, J. He, J. Zhao, X. Xiong, Disulfide stabilization reveals conserved dynamic features between SARS-CoV-1 and SARS-CoV-2 spikes. *Life Sci. Alliance* **6**, e202201796 (2023).
17. R. N. Kirchdoerfer, N. Wang, J. Pallesen, D. Wrapp, H. L. Turner, C. A. Cottrell, K. S. Corbett, B. S. Graham, J. S. McLellan, A. B. Ward, Publisher Correction: Stabilized coronavirus spikes are resistant to conformational changes induced by receptor recognition or proteolysis. *Sci. Rep.* **8**, 17823 (2018).
18. A. C. Walls, X. Xiong, Y.-J. Park, M. A. Tortorici, J. Snijder, J. Quispe, E. Cameroni, R. Gopal, M. Dai, A. Lanzavecchia, M. Zambon, F. A. Rey, D. Corti, D. Veesler, Unexpected receptor functional mimicry elucidates activation of coronavirus fusion. *Cell* **183**, 1732 (2020).
19. Y. Yuan, D. Cao, Y. Zhang, J. Ma, J. Qi, Q. Wang, G. Lu, Y. Wu, J. Yan, Y. Shi, X. Zhang, G. F. Gao, Cryo-EM structures of MERS-CoV and SARS-CoV spike glycoproteins reveal the dynamic receptor binding domains. *Nat. Commun.* **8**, 15092 (2017).
20. D. J. Benton, A. G. Wrobel, P. Xu, C. Roustan, S. R. Martin, P. B. Rosenthal, J. J. Skehel, S. J. Gamblin, Receptor binding and priming of the spike protein of SARS-CoV-2 for membrane fusion. *Nature* **588**, 327–330 (2020).
21. S. Bangaru, G. Ozorowski, H. L. Turner, A. Antanasijevic, D. Huang, X. Wang, J. L. Torres, J. K. Diedrich, J.-H. Tian, A. D. Portnoff, N. Patel, M. J. Massare, J. R. Yates III, D. Nemazee, J. C. Paulson, G. Glenn, G. Smith, A. B. Ward, Structural analysis of full-length SARS-CoV-2 spike protein from an advanced vaccine candidate. *Science* **370**, 1089–1094 (2020).
22. A. C. Walls, Y.-J. Park, M. A. Tortorici, A. Wall, A. T. McGuire, D. Veesler, Structure, function, and antigenicity of the SARS-CoV-2 spike glycoprotein. *Cell* **183**, 1735 (2020).
23. D. Wrapp, N. Wang, K. S. Corbett, J. A. Goldsmith, C.-L. Hsieh, O. Abiona, B. S. Graham, J. S. McLellan, Cryo-EM structure of the 2019-nCoV spike in the prefusion conformation. *Science* **367**, 1260–1263 (2020).
24. X. Xiong, K. Qu, K. A. Ciazynska, M. Hosmillo, A. P. Carter, S. Ebrahimi, Z. Ke, S. H. W. Scheres, L. Bergamaschi, G. L. Grice, Y. Zhang, The CITIID-NIHR COVID-19 BioResource Collaboration, J. A. Nathan, S. Baker, L. C. James, H. E. Baxendale, I. Goodfellow, R. Doffinger, J. A. G. Briggs, A thermostable, closed SARS-CoV-2 spike protein trimer. *Nat. Struct. Mol. Biol.* **27**, 934–941 (2020).
25. C. Toelzer, K. Gupta, S. K. N. Yadav, L. Hodgson, M. K. Williamson, D. Buzas, U. Borucu, K. Powers, R. Stenner, K. Vasileiou, F. Garzoni, D. Fitzgerald, C. Payré, G. Gautam, G. Lambeau, A. D. Davidson, P. Verkade, M. Frank, I. Berger, C. Schaffitzel, The free fatty acid–binding pocket is a conserved hallmark in pathogenic β-coronavirus spike proteins from SARS-CoV to Omicron. *Sci. Adv.* **8**, eadc9179 (2022).
26. S. Zhang, S. Qiao, J. Yu, J. Zeng, S. Shan, L. Tian, J. Lan, L. Zhang, X. Wang, Bat and pangolin coronavirus spike glycoprotein structures provide insights into SARS-CoV-2 evolution. *Nat. Commun.* **12**, 1607 (2021).
27. A. G. Wrobel, D. J. Benton, P. Xu, L. J. Calder, A. Borg, C. Roustan, S. R. Martin, P. B. Rosenthal, J. J. Skehel, S. J. Gamblin, Structure and binding properties of Pangolin-CoV spike glycoprotein inform the evolution of SARS-CoV-2. *Nat. Commun.* **12**, 837 (2021).
28. K. Qu, Q. Chen, K. A. Ciazynska, B. Liu, X. Zhang, J. Wang, Y. He, J. Guan, J. He, T. Liu, X. Zhang, A. P. Carter, X. Xiong, J. A. G. Briggs, Engineered disulfide reveals structural dynamics of locked SARS-CoV-2 spike. *PLOS Pathog.* **18**, e1010583 (2022).
29. Z. Ke, J. Oton, K. Qu, M. Cortese, V. Zila, L. McKeane, T. Nakane, J. Zivanov, C. J. Neufeldt, B. Cerikan, J. M. Lu, J. Peukes, X. Xiong, H.-G. Krausslich, S. H. W. Scheres, R. Bartenschlager, J. A. G. Briggs, Structures and distributions of SARS-CoV-2 spike proteins on intact virions. *Nature* **588**, 498–502 (2020).
30. Y. Cai, J. Zhang, T. Xiao, H. Peng, S. M. Sterling, R. M. Walsh Jr., S. Rawson, S. Rits-Volloch, B. Chen, Distinct conformational states of SARS-CoV-2 spike protein. *Science* **369**, 1586–1592 (2020).
31. A. C. Walls, X. Xiong, Y.-J. Park, M. A. Tortorici, J. Snijder, J. Quispe, E. Cameroni, R. Gopal, M. Dai, A. Lanzavecchia, M. Zambon, F. A. Rey, D. Corti, D. Veesler, Unexpected receptor functional mimicry elucidates activation of coronavirus fusion. *Cell* **176**, 1026–1039.e15 (2019).
32. W. Li, Z. Shi, M. Yu, W. Ren, C. Smith, J. H. Epstein, H. Wang, G. Crameri, Z. Hu, H. Zhang, J. Zhang, J. McEachern, H. Field, P. Daszak, B. T. Eaton, S. Zhang, L.-F. Wang, Bats are natural reservoirs of SARS-like coronaviruses. *Science* **310**, 676–679 (2005).
33. X.-Y. Ge, J.-L. Li, X.-L. Yang, A. A. Chmura, G. Zhu, J. H. Epstein, J. K. Mazet, B. Hu, W. Zhang, C. Peng, Y.-J. Zhang, C.-M. Luo, B. Tan, N. Wang, Y. Zhu, G. Crameri, S.-Y. Zhang, L.-F. Wang, P. Daszak, Z.-L. Shi, Isolation and characterization of a bat SARS-like coronavirus that uses the ACE2 receptor. *Nature* **503**, 535–538 (2013).
34. K. Xiao, J. Zhai, Y. Feng, N. Zhou, X. Zhang, J.-J. Zou, N. Li, Y. Guo, X. Li, X. Shen, Z. Zhang, F. Shu, W. Huang, Y. Li, Z. Zhang, R.-A. Chen, Y.-J. Wu, S.-M. Peng, M. Huang, W.-J. Xie, Q.-H. Cai, F.-H. Hou, W. Chen, L. Xiao, Y. Shen, Isolation of SARS-CoV-2-related coronavirus from Malayan pangolins. *Nature* **583**, 286–289 (2020).
35. P. C. Y. Woo, S. K. P. Lau, K. S. M. Li, R. W. S. Poon, B. H. L. Wong, H.-W. Tsoi, B. C. K. Yip, Y. Huang, K.-H. Chan, K.-Y. Yuen, Molecular diversity of coronaviruses in bats. *Virology* **351**, 180–187 (2006).
36. Y. Guan, B. J. Zheng, Y. Q. He, X. L. Liu, Z. X. Zhuang, C. L. Cheung, S. W. Luo, P. H. Li, L. J. Zhang, Y. J. Guan, K. M. Butt, K. L. Wong, K. W. Chan, W. Lim, K. F. Shortridge, K. Y. Yuen, J. S. M. Peiris, L. L. M. Poon, Isolation and characterization of viruses related to the SARS coronavirus from animals in southern China. *Science* **302**, 276–278 (2003).
37. K. Liu, X. Pan, L. Li, F. Yu, A. Zheng, P. Du, P. Han, Y. Meng, Y. Zhang, L. Wu, Q. Chen, C. Song, Y. Jia, S. Niu, D. Lu, C. Qiao, Z. Chen, D. Ma, X. Ma, S. Tan, X. Zhao, J. Qi, G. F. Gao, Q. Wang, Binding and molecular basis of the bat coronavirus RaTG13 virus to ACE2 in humans and other species. *Cell* **184**, 3438–3451.e10 (2021).
38. H.-D. Song, C.-C. Tu, G.-W. Zhang, S.-Y. Wang, K. Zheng, L.-C. Lei, Q.-X. Chen, Y.-W. Gao, H.-Q. Zhou, H. Xiang, H.-J. Zheng, S.-W. W. Chern, F. Cheng, C.-M. Pan, H. Xuan, S.-J. Chen, H.-M. Luo, D.-H. Zhou, Y.-F. Liu, J.-F. He, P.-Z. Qin, L.-H. Li, Y.-Q. Ren, W.-J. Liang, Y.-D. Yu, L. Anderson, M. Wang, R.-H. Xu, X.-W. Wu, H.-Y. Zheng, J.-D. Chen, G. Liang, Y. Gao, M. Liao, L. Fang, L.-Y. Jiang, H. Li, F. Chen, B. Di, L.-J. He, J.-Y. Lin, S. Tong, X. Kong, L. Du, P. Hao, H. Tang, A. Bernini, X.-J. Yu, O. Spiga, Z.-M. Guo, H.-Y. Pan, W.-Z. He, J.-C. Manuguerra, A. Fontanet, A. Danchin, N. Niccolai, Y.-X. Li, C.-I. Wu, G.-P. Zhao, Cross-host evolution of severe acute respiratory syndrome coronavirus in palm civet and human. *Proc. Natl. Acad. Sci. U.S.A.* **102**, 2430–2435 (2005).
39. J. M. Crook, I. Murphy, D. P. Carter, S. T. Pullan, M. Carroll, R. Vipond, A. A. Cunningham, D. Bell, Metagenomic identification of a new sarbecovirus from horseshoe bats in Europe. *Sci. Rep.* **11**, 14723 (2021).
40. S. Temmam, K. Vongphayloth, E. Baquero, S. Munier, M. Bonomi, B. Regnault, B. Douangboubpha, Y. Karami, D. Chretien, D. Sanamxay, V. Xayaphet, P. Paphaphanh, V. Lacoste, S. Somlor, K. Lakeomany, N. Phommavanh, P. Perot, O. Dehan, F. Amara, F. Donati, T. Bigot, M. Nilges, F. A. Rey, S. van der Werf, P. T. Brey, M. Eloit, Bat coronaviruses related to SARS-CoV-2 and infectious for human cells. *Nature* **604**, 330–336 (2022).

41. W. Markotter, M. Geldenhuys, P. Jansen van Vuren, A. Kemp, M. Mortlock, A. Mudakikwa, L. Nel, J. Nziza, J. Paweska, J. Weyer, Paramyxo- and coronaviruses in Rwandan bats. *Trop. Med. Infect. Dis.* **4**, 99 (2019).
42. S. Alkhovsky, S. Lenshin, A. Romashin, T. Vishnevskaya, O. Vyshemirsky, Y. Bulycheva, D. Lvov, A. Gitelman, SARS-like coronaviruses in horseshoe bats (*Rhinolophus* spp.) in Russia, 2020. *Viruses* **14**, 113 (2022).
43. H. Zhou, J. Ji, X. Chen, Y. Bi, J. Li, Q. Wang, T. Hu, H. Song, R. Zhao, Y. Chen, M. Cui, Y. Zhang, A. C. Hughes, E. C. Holmes, W. Shi, Identification of novel bat coronaviruses sheds light on the evolutionary origins of SARS-CoV-2 and related viruses. *Cell* **184**, 4380–4391.e14 (2021).
44. D. Delaune, V. Hul, E. A. Karlsson, A. Hassanin, T. P. Ou, A. Baidaliuk, F. Gambaro, M. Prot, V. T. Tu, S. Chea, L. Keatts, J. Mazet, C. K. Johnson, P. Buchy, P. Dussart, T. Goldstein, E. Simon-Loriere, V. Duong, A novel SARS-CoV-2 related coronavirus in bats from Cambodia. *Nat. Commun.* **12**, 6563 (2021).
45. S. Murakami, T. Kitamura, J. Suzuki, R. Sato, T. Aoi, M. Fujii, H. Matsugo, H. Kamiki, H. Ishida, A. Takenaka-Uema, M. Shimojima, T. Horimoto, Detection and characterization of bat sarbecovirus phylogenetically related to SARS-CoV-2, Japan. *Emerg. Infect. Dis.* **26**, 3025–3029 (2020).
46. B. He, Y. Zhang, L. Xu, W. Yang, F. Yang, Y. Feng, L. Xia, J. Zhou, W. Zhen, Y. Feng, H. Guo, H. Zhang, C. Tu, Identification of diverse alphacoronaviruses and genomic characterization of a novel severe acute respiratory syndrome-like coronavirus from bats in China. *J. Virol.* **88**, 7070–7082 (2014).
47. H. Guo, A. Li, T.-Y. Dong, H.-R. Si, B. Hu, B. Li, Y. Zhu, Z.-L. Shi, M. Letko, Isolation of ACE2-dependent and -independent sarbecoviruses from Chinese horseshoe bats. *J. Virol.* **97**, e0039523 (2023).
48. H. Guo, A. Li, T.-Y. Dong, J. Su, Y.-L. Yao, Y. Zhu, Z.-L. Shi, M. Letko, ACE2-independent bat sarbecovirus entry and replication in human and bat cells. *mBio* **13**, e0256622 (2022).
49. B. Hu, H. Guo, H. Si, Z. Shi, Emergence of SARS and COVID-19 and preparedness for the next emerging disease X. *Front. Med.* **18**, 1–18 (2024).
50. H. L. Wells, M. Letko, G. Lasso, B. Ssebide, J. Nziza, D. K. Byarugaba, I. Navarrete-Macias, E. Liang, M. Cranfield, B. A. Han, M. W. Tingley, M. Diuk-Wasser, T. Goldstein, C. K. Johnson, J. A. K. Mazet, K. Chandran, V. J. Munster, K. Gilardi, S. J. Anthony, The evolutionary history of ACE2 usage within the coronavirus subgenus Sarbecovirus. *Virus Evol.* **7**, veab007 (2021).
51. Z. Wu, L. Yang, X. Ren, G. He, J. Zhang, J. Yang, Z. Qian, J. Dong, L. Sun, Y. Zhu, J. Du, F. Yang, S. Zhang, Q. Jin, Deciphering the bat virome catalog to better understand the ecological diversity of bat viruses and the bat origin of emerging infectious diseases. *ISME J.* **10**, 609–620 (2016).
52. H. Zhou, X. Chen, T. Hu, J. Li, H. Song, Y. Liu, P. Wang, D. Liu, J. Yang, E. C. Holmes, A. C. Hughes, Y. Bi, W. Shi, A novel bat coronavirus closely related to SARS-CoV-2 contains natural insertions at the S1/S2 cleavage site of the spike protein. *Curr. Biol.* **30**, 2196–2203.e3 (2020).
53. S. Tong, C. Conrardy, S. Ruone, I. V. Kuzmin, X. Guo, Y. Tao, M. Niezgoda, L. Haynes, B. Agwanda, R. F. Breiman, L. J. Anderson, C. E. Rupprecht, Detection of novel SARS-like and other coronaviruses in bats from Kenya. *Emerg. Infect. Dis.* **15**, 482–485 (2009).
54. J. F. Drexler, F. Gloza-Rausch, J. Glende, V. M. Corman, D. Muth, M. Goettsche, A. Seebens, M. Niedrig, S. Pfefferle, S. Yordanov, L. Zhelyazkov, U. Hermanns, P. Vallo, A. Lukashev, M. A. Muller, H. Deng, G. Herrler, C. Drosten, Genomic characterization of severe acute respiratory syndrome-related coronavirus in European bats and classification of coronaviruses based on partial RNA-dependent RNA polymerase gene sequences. *J. Virol.* **84**, 11336–11349 (2010).
55. T. Zhou, Y. Tsybovsky, J. Gorman, M. Rapp, G. Cerutti, G. Y. Chuang, P. S. Katsamba, J. M. Sampson, A. Schon, J. Bimela, J. C. Boyington, A. Nazzari, A. S. Olia, W. Shi, M. Sastry, T. Stephens, J. Stuckey, I. T. Teng, P. Wang, S. Wang, B. Zhang, R. A. Friesner, D. D. Ho, J. R. Mascola, L. Shapiro, P. D. Kwong, Cryo-EM structures of SARS-CoV-2 spike without and with ACE2 reveal a pH-dependent switch to mediate endosomal positioning of receptor-binding domains. *Cell Host Microbe* **28**, 867–879.e5 (2020).
56. S. B. Egri, X. Wang, M. A. Diaz-Salinas, J. Luban, N. V. Dudkina, J. B. Munro, K. Shen, Detergent modulates the conformational equilibrium of SARS-CoV-2 Spike during cryo-EM structural determination. *Nat. Commun.* **14**, 2527 (2023).
57. W. Shi, Y. Cai, H. Zhu, H. Peng, J. Voyer, S. Rits-Volloch, H. Cao, M. L. Mayer, K. Song, C. Xu, J. Lu, J. Zhang, B. Chen, Cryo-EM structure of SARS-CoV-2 postfusion spike in membrane. *Nature* **619**, 403–409 (2023).
58. M. M. Zhao, Y. Zhu, L. Zhang, G. Zhong, L. Tai, S. Liu, G. Yin, J. Lu, Q. He, M. J. Li, R. X. Zhao, H. Wang, W. Huang, C. Fan, L. Shuai, Z. Wen, C. Wang, X. He, Q. Chen, B. Liu, X. Xiong, Z. Bu, Y. Wang, F. Sun, J. K. Yang, Novel cleavage sites identified in SARS-CoV-2 spike protein reveal mechanism for cathepsin L-facilitated viral infection and treatment strategies. *Cell Discov.* **8**, 53 (2022).
59. X. Ou, G. Xu, P. Li, Y. Liu, F. Zan, P. Liu, J. Hu, X. Lu, S. Dong, Y. Zhou, Z. Mu, Z. Wu, J. Wang, Q. Jin, P. Liu, J. Lu, X. Wang, Z. Qian, Host susceptibility and structural and immunological insight of S proteins of two SARS-CoV-2 closely related bat coronaviruses. *Cell Discov.* **9**, 78 (2023).
60. J. Lee, S. K. Zepeda, Y. J. Park, A. L. Taylor, J. Quispe, C. Stewart, E. M. Leaf, C. Treichel, D. Corti, N. P. King, T. N. Starr, D. Veesler, Broad receptor tropism and immunogenicity of a clade 3 sarbecovirus. *Cell Host Microbe* **31**, 1961–1973.e11 (2023).
61. C. Toelzer, K. Gupta, S. K. N. Yadav, U. Borucu, A. D. Davidson, M. Kavanagh Williamson, D. K. Shoemark, F. Garzoni, O. Staufer, R. Milligan, J. Capin, A. J. Mulholland, J. Spatz, D. Fitzgerald, I. Berger, C. Schaffitzel, Free fatty acid binding pocket in the locked structure of SARS-CoV-2 spike protein. *Science* **370**, 725–730 (2020).
62. W. T. Harvey, A. M. Carabelli, B. Jackson, R. K. Gupta, E. C. Thomson, E. M. Harrison, C. Ludden, R. Reeve, A. Rambaut, COVID-19 Genomics UK (COG-UK) Consortium, S. J. Peacock, D. L. Robertson, SARS-CoV-2 variants, spike mutations and immune escape. *Nat. Rev. Microbiol.* **19**, 409–424 (2021).
63. M. McCallum, A. De Marco, F. A. Lempp, M. A. Tortorici, D. Pinto, A. C. Walls, M. Beltramello, A. Chen, Z. Liu, F. Zatta, S. Zepeda, J. di Iulio, J. E. Bowen, M. Montiel-Ruiz, J. Zhou, L. E. Rosen, S. Bianchi, B. Guarino, C. S. Fregni, R. Abdelnabi, S. C. Foo, P. W. Rothlauf, L. M. Bloyet, F. Benigni, E. Cameroni, J. Neyts, A. Riva, G. Snell, A. Telenti, S. P. J. Whelan, H. W. Virgin, D. Corti, M. S. Pizzuto, D. Veesler, N-terminal domain antigenic mapping reveals a site of vulnerability for SARS-CoV-2. *Cell* **184**, 2332–2347.e16 (2021).
64. L. E. Rosen, M. A. Tortorici, A. De Marco, D. Pinto, W. B. Foreman, A. L. Taylor, Y. J. Park, D. Bohan, T. Rietz, J. M. Errico, K. Hauser, H. V. Dang, J. W. Chartron, M. Giurdanella, G. Cusumano, C. Saliba, F. Zatta, K. R. Sprouse, A. Addetia, S. K. Zepeda, J. Brown, J. Lee, E. Dellota Jr., A. Rajesh, J. Noack, Q. Tao, Y. DaCosta, B. Tsu, R. Acosta, S. Subramanian, G. D. de Melo, L. Kergoat, I. Zhang, Z. Liu, B. Guarino, M. A. Schmid, G. Schnell, J. L. Miller, F. A. Lempp, N. Czudnochowski, E. Cameroni, S. P. J. Whelan, H. Bourhy, L. A. Purcell, F. Benigni, J. di Iulio, M. S. Pizzuto, A. Lanzavecchia, A. Telenti, G. Snell, D. Corti, D. Veesler, T. N. Starr, A potent pan-sarbecovirus neutralizing antibody resilient to epitope diversification. *Cell* **187**, 7196–7213.e26 (2024).
65. Y. Cao, F. Jian, Z. Zhang, A. Yisimayi, X. Hao, L. Bao, F. Yuan, Y. Yu, S. Du, J. Wang, T. Xiao, W. Song, Y. Zhang, P. Liu, R. An, P. Wang, Y. Wang, S. Yang, X. Niu, Y. Zhang, Q. Gu, F. Shao, Y. Hu, W. Yin, A. Zheng, Y. Wang, C. Qin, R. Jin, J. Xiao, X. S. Xie, Rational identification of potent and broad sarbecovirus-neutralizing antibody cocktails from SARS convalescents. *Cell Rep.* **41**, 111845 (2022).
66. A. M. Carabelli, T. P. Peacock, L. G. Thorne, W. T. Harvey, J. Hughes, COVID-19 Genomics UK Consortium, S. J. Peacock, W. S. Barclay, T. I. de Silva, G. J. Towers, D. L. Robertson, SARS-CoV-2 variant biology: Immune escape, transmission and fitness. *Nat. Rev. Microbiol.* **21**, 162–177 (2023).
67. H. Yu, B. Liu, Y. Zhang, X. Gao, Q. Wang, H. Xiang, X. Peng, C. Xie, Y. Wang, P. Hu, J. Shi, Q. Shi, P. Zheng, C. Feng, G. Tang, X. Liu, L. Guo, X. Lin, J. Li, C. Liu, Y. Huang, N. Yang, Q. Chen, Z. Li, M. Su, Q. Yan, R. Pei, X. Chen, L. Liu, F. Hu, D. Liang, B. Ke, C. Ke, F. Li, J. He, M. Wang, L. Chen, X. Xiong, X. Tang, Somatically hypermutated antibodies isolated from SARS-CoV-2 Delta infected patients cross-neutralize heterologous variants. *Nat. Commun.* **14**, 1058 (2023).
68. Q. Yan, Y. Zhang, R. Hou, W. Pan, H. Liang, X. Gao, W. Deng, X. Huang, L. Qu, C. Tang, P. He, B. Liu, Q. Wang, X. Zhao, Z. Lin, Z. Chen, P. Li, J. Han, X. Xiong, J. Zhao, S. Li, X. Niu, L. Chen, Deep immunoglobulin repertoire sequencing depicts a comprehensive atlas of spike-specific antibody lineages shared among COVID-19 convalescents. *Emerg. Microbes Infect.* **13**, 2290841 (2024).
69. B. Liu, X. Niu, Y. Deng, Z. Zhang, Y. Wang, X. Gao, H. Liang, Z. Li, Q. Wang, Y. Cheng, Q. Chen, S. Huang, Y. Pan, M. Su, X. Lin, C. Niu, Y. Chen, W. Yang, Y. Zhang, Q. Yan, J. He, J. Zhao, L. Chen, X. Xiong, An unconventional VH1-2 antibody tolerates escape mutations and shows an antigenic hotspot on SARS-CoV-2 spike. *Cell Rep.* **43**, 114265 (2024).
70. J. Dong, S. J. Zost, A. J. Greaney, T. N. Starr, A. S. Dingens, E. C. Chen, R. E. Chen, J. B. Case, R. E. Sutton, P. Gilchuk, J. Rodriguez, E. Armstrong, C. Gainza, R. S. Nargi, E. Binshtein, X. Xie, X. Zhang, P. Y. Shi, J. Logue, S. Weston, M. E. McGrath, M. B. Frieman, T. Brady, K. M. Tuffy, H. Bright, Y. M. Loo, P. M. McTamney, M. T. Esser, R. H. Carnahan, M. S. Diamond, J. D. Bloom, J. E. Crowe Jr., Genetic and structural basis for SARS-CoV-2 variant neutralization by a two-antibody cocktail. *Nat. Microbiol.* **6**, 1233–1244 (2021).
71. M. Yuan, Y. Wang, H. Lv, T. J. C. Tan, I. A. Wilson, N. C. Wu, Molecular analysis of a public cross-neutralizing antibody response to SARS-CoV-2. *Cell Rep.* **41**, 111650 (2022).
72. Q. Yan, R. Hou, X. Huang, Y. Zhang, P. He, Y. Zhang, B. Liu, Q. Wang, H. Rao, X. Chen, X. Zhao, X. Niu, J. Zhao, X. Xiong, L. Chen, Shared IGHV1-69-encoded neutralizing antibodies contribute to the emergence of L452R substitution in SARS-CoV-2 variants. *Emerg. Microbes Infect.* **11**, 2749–2761 (2022).
73. P. He, B. Liu, X. Gao, Q. Yan, R. Pei, J. Sun, Q. Chen, R. Hou, Z. Li, Y. Zhang, J. Zhao, H. Sun, B. Feng, Q. Wang, H. Yi, P. Hu, P. Li, Y. Zhang, Z. Chen, X. Niu, X. Zhong, L. Jin, X. Liu, K. Qu, K. A. Ciazynska, A. P. Carter, J. A. G. Briggs, J. Chen, J. Liu, X. Chen, J. He, L. Chen, X. Xiong, SARS-CoV-2 Delta and Omicron variants evade population antibody response by mutations in a single spike epitope. *Nat. Microbiol.* **7**, 1635–1649 (2022).
74. M. Yuan, D. Huang, C. D. Lee, N. C. Wu, A. M. Jackson, X. Zhu, H. Liu, L. Peng, M. J. van Gils, R. W. Sanders, D. R. Burton, S. M. Reincke, H. Pruss, J. Kreye, D. Nemazee, A. B. Ward, I. A. Wilson, Structural and functional ramifications of antigenic drift in recent SARS-CoV-2 variants. *Science* **373**, 818–823 (2021).

75. M. Rapp, Y. Guo, E. R. Reddem, J. Yu, L. Liu, P. Wang, G. Cerutti, P. Katsamba, J. S. Bimela, F. A. Bahna, S. M. Mannepalli, B. Zhang, P. D. Kwong, Y. Huang, D. D. Ho, L. Shapiro, Z. Sheng, Modular basis for potent SARS-CoV-2 neutralization by a prevalent VH1-2-derived antibody class. *Cell Rep.* **35**, 108950 (2021).
76. Q. Yan, P. He, X. Huang, K. Luo, Y. Zhang, H. Yi, Q. Wang, F. Li, R. Hou, X. Fan, P. Li, X. Liu, H. Liang, Y. Deng, Z. Chen, Y. Chen, X. Mo, L. Feng, X. Xiong, S. Li, J. Han, L. Qu, X. Niu, L. Chen, Germline IGHV3-53-encoded RBD-targeting neutralizing antibodies are commonly present in the antibody repertoires of COVID-19 patients. *Emerg. Microbes Infect.* **10**, 1097–1111 (2021).
77. S. Zhang, Q. Liang, X. He, C. Zhao, W. Ren, Z. Yang, Z. Wang, Q. Ding, H. Deng, T. Wang, L. Zhang, X. Wang, Loss of Spike N370 glycosylation as an important evolutionary event for the enhanced infectivity of SARS-CoV-2. *Cell Res.* **32**, 315–318 (2022).
78. A. M. Harbison, C. A. Fogarty, T. K. Phung, A. Satheesan, B. L. Schulz, E. Fadda, Fine-tuning the spike: Role of the nature and topology of the glycan shield in the structure and dynamics of the SARS-CoV-2 S. *Chem. Sci.* **13**, 386–395 (2022).
79. T. Sztain, S. H. Ahn, A. T. Bogetti, L. Casalino, J. A. Goldsmith, E. Seitz, R. S. McCool, F. L. Kearns, F. Acosta-Reyes, S. Maji, G. Mashayekhi, J. A. McCammon, A. Ourmazd, J. Frank, J. S. McLellan, L. T. Chong, R. E. Amaro, A glycan gate controls opening of the SARS-CoV-2 spike protein. *Nat. Chem.* **13**, 963–968 (2021).
80. S. Qiao, S. Zhang, J. Ge, X. Wang, The spike glycoprotein of highly pathogenic human coronaviruses: Structural insights for understanding infection, evolution and inhibition. *FEBS Open Bio* **12**, 1602–1622 (2022).
81. Y. Watanabe, Z. T. Berndsen, J. Raghwani, G. E. Seabright, J. D. Allen, O. G. Pybus, J. S. McLellan, I. A. Wilson, T. A. Bowden, A. B. Ward, M. Crispin, Vulnerabilities in coronavirus glycan shields despite extensive glycosylation. *Nat. Commun.* **11**, 2688 (2020).
82. J. D. Allen, D. P. Ivory, S. G. Song, W. T. He, T. Capozzola, P. Yong, D. R. Burton, R. Andrabi, M. Crispin, The diversity of the glycan shield of sarbecoviruses related to SARS-CoV-2. *Cell Rep.* **42**, 112307 (2023).
83. Y. Ma, P. Li, Y. Hu, T. Qiu, L. Wang, H. Lu, K. Lv, M. Xu, J. Zhuang, X. Liu, S. He, B. He, S. Liu, L. Liu, Y. Wang, X. Yue, Y. Zhai, W. Luo, H. Mai, Y. Kuang, S. Chen, F. Ye, N. Zhou, W. Zhao, J. Chen, S. Chen, X. Xiong, M. Shi, J.-A. Pan, Y.-Q. Chen, Spike substitution T813S increases Sarbecovirus fusogenicity by enhancing the usage of TMPRSS2. *PLOS Pathog.* **19**, e1011123 (2023).
84. T. N. Starr, S. K. Zepeda, A. C. Walls, A. J. Greaney, S. Alkhovsky, D. Veesler, J. D. Bloom, ACE2 binding is an ancestral and evolvable trait of sarbecoviruses. *Nature* **603**, 913–918 (2022).
85. P. Towler, B. Staker, S. G. Prasad, S. Menon, J. Tang, T. Parsons, D. Ryan, M. Fisher, D. Williams, N. A. Dales, M. A. Patane, M. W. Pantoliano, ACE2 X-ray structures reveal a large hinge-bending motion important for inhibitor binding and catalysis. *J. Biol. Chem.* **279**, 17996–18007 (2004).
86. R. Yan, Y. Zhang, Y. Li, L. Xia, Y. Guo, Q. Zhou, Structural basis for the recognition of SARS-CoV-2 by full-length human ACE2. *Science* **367**, 1444–1448 (2020).
87. C. Su, J. He, L. Wang, Y. Hu, J. Cao, B. Bai, J. Qi, G. F. Gao, M. Yang, Q. Wang, Structural characteristics of BtKY72 RBD bound to bat ACE2 reveal multiple key residues affecting ACE2 usage of sarbecoviruses. *mBio* **15**, e0140424 (2024).
88. P. Han, C. Su, Y. Zhang, C. Bai, A. Zheng, C. Qiao, Q. Wang, S. Niu, Q. Chen, Y. Zhang, W. Li, H. Liao, J. Li, Z. Zhang, H. Cho, M. Yang, X. Rong, Y. Hu, N. Huang, J. Yan, Q. Wang, X. Zhao, G. F. Gao, J. Qi, Molecular insights into receptor binding of recent emerging SARS-CoV-2 variants. *Nat. Commun.* **12**, 6103 (2021).
89. L. Li, H. Liao, Y. Meng, W. Li, P. Han, K. Liu, Q. Wang, D. Li, Y. Zhang, L. Wang, Z. Fan, Y. Zhang, Q. Wang, X. Zhao, Y. Sun, N. Huang, J. Qi, G. F. Gao, Structural basis of human ACE2 higher binding affinity to currently circulating Omicron SARS-CoV-2 sub-variants BA.2 and BA.1.1. *Cell* **185**, 2952–2960.e10 (2022).
90. K. H. Dinnon III, S. R. Leist, A. Schäfer, C. E. Edwards, D. R. Martinez, S. A. Montgomery, A. West, B. L. Yount Jr., Y. J. Hou, L. E. Adams, K. L. Gully, A. J. Brown, E. Huang, M. D. Bryant, I. C. Choong, J. S. Glenn, L. E. Gralinski, T. P. Sheahan, R. S. Baric, A mouse-adapted model of SARS-CoV-2 to test COVID-19 countermeasures. *Nature* **586**, 560–566 (2020).
91. Q. Wang, S. Noettger, Q. Xie, C. Pastorio, A. Seidel, J. A. Muller, C. Jung, T. Jacob, K. M. J. Sparrer, F. Zech, F. Kirchhoff, Determinants of species-specific utilization of ACE2 by human and animal coronaviruses. *Commun. Biol.* **6**, 1051 (2023).
92. M. Letko, A. Marzi, V. Munster, Functional assessment of cell entry and receptor usage for SARS-CoV-2 and other lineage B betacoronaviruses. *Nat. Microbiol.* **5**, 562–569 (2020).
93. J. Y. Si, Y. M. Chen, Y. H. Sun, M. X. Gu, M. L. Huang, L. L. Shi, X. Yu, X. Yang, Q. Xiong, C. B. Ma, P. Liu, Z. L. Shi, H. Yan, Sarbecovirus RBD indels and specific residues dictating multi-species ACE2 adaptiveness. *Nat. Commun.* **15**, 8869 (2024).
94. F. Li, Structural analysis of major species barriers between humans and palm civets for severe acute respiratory syndrome coronavirus infections. *J. Virol.* **82**, 6984–6991 (2008).
95. W. Li, C. Zhang, J. Sui, J. H. Kuhn, M. J. Moore, S. Luo, S. K. Wong, I. C. Huang, K. Xu, N. Vasilieva, A. Murakami, Y. He, W. A. Marasco, Y. Guan, H. Choe, M. Farzan, Receptor and viral determinants of SARS-coronavirus adaptation to human ACE2. *EMBO J.* **24**, 1634–1643 (2005).
96. M. R. Heindl, E. Böttcher-Friebertshäuser, The role of influenza-A virus and coronavirus viral glycoprotein cleavage in host adaptation. *Curr. Opin. Virol.* **58**, 101303 (2023).
97. A. Rosa, V. E. Pye, C. Graham, L. Muir, J. Seow, K. W. Ng, N. J. Cook, C. Rees-Spear, E. Parker, M. S. Dos Santos, C. Rosadas, A. Susana, H. Rhys, A. Nans, L. Masino, C. Roustan, E. Christodoulou, R. Ulferts, A. G. Wrobel, C. E. Short, M. Fertleman, R. W. Sanders, J. Heaney, M. Spyer, S. Kjær, A. Riddell, M. H. Malim, R. Beale, J. I. MacRae, G. P. Taylor, E. Nastouli, M. J. van Gils, P. B. Rosenthal, M. Pizzato, M. O. McClure, R. S. Tedder, G. Kassiotis, L. E. McCoy, K. J. Doores, P. Cherepanov, SARS-CoV-2 can recruit a heme metabolite to evade antibody immunity. *Sci. Adv.* **7**, eabg7607 (2021).
98. S. L. Freeman, A. S. F. Oliveira, A. E. Gallio, A. Rosa, M. K. Simitakou, C. J. Arthur, A. J. Mulholland, P. Cherepanov, E. L. Raven, Heme binding to the SARS-CoV-2 spike glycoprotein. *J. Biol. Chem.* **299**, 105014 (2023).
99. T. J. Yang, P. Y. Yu, Y. C. Chang, S. D. Hsu, D614G mutation in the SARS-CoV-2 spike protein enhances viral fitness by desensitizing it to temperature-dependent denaturation. *J. Biol. Chem.* **297**, 101238 (2021).
100. W. Ren, X. Qu, W. Li, Z. Han, M. Yu, P. Zhou, S. Y. Zhang, L. F. Wang, H. Deng, Z. Shi, Difference in receptor usage between severe acute respiratory syndrome (SARS) coronavirus and SARS-like coronavirus of bat origin. *J. Virol.* **82**, 1899–1907 (2008).
101. H. Guo, B. Hu, H.-R. Si, Y. Zhu, W. Zhang, B. Li, A. Li, R. Geng, H.-F. Lin, X. L. Yang, P. Zhou, Z.-L. Shi, Identification of a novel lineage bat SARS-related coronaviruses that use bat ACE2 receptor. *Emerg. Microbes Infect.* **10**, 1507–1514 (2021).
102. S. M. Roelle, N. Shukla, A. T. Pham, A. M. Bruchez, K. A. Matreyek, Expanded ACE2 dependencies of diverse SARS-like coronavirus receptor binding domains. *PLoS Biol.* **20**, e3001738 (2022).
103. D. Ni, P. Turelli, B. Beckert, S. Nazarov, E. Uchikawa, A. Myasnikov, F. Pojer, D. Trono, H. Stahlberg, K. Lau, Cryo-EM structures and binding of mouse and human ACE2 to SARS-CoV-2 variants of concern indicate that mutations enabling immune escape could expand host range. *PLOS Pathog.* **19**, e1011206 (2023).
104. Y. Hu, K. Liu, P. Han, Z. Xu, A. Zheng, X. Pan, Y. Jia, C. Su, L. Tang, L. Wu, B. Bai, X. Zhao, D. Tian, Z. Chen, J. Qi, Q. Wang, G. F. Gao, Host range and structural analysis of bat-origin RshSTT182/200 coronavirus binding to human ACE2 and its animal orthologs. *EMBO J.* **42**, e111737 (2023).
105. J. Pallesen, N. Wang, K. S. Corbett, D. Wrapp, R. N. Kirchdoerfer, H. L. Turner, C. A. Cottrell, M. M. Becker, L. Wang, W. Shi, W. P. Kong, E. L. Andres, A. N. Kettenbach, M. R. Denison, J. D. Chappell, B. S. Graham, A. B. Ward, J. S. McLellan, Immunogenicity and structures of a rationally designed prefusion MERS-CoV spike antigen. *Proc. Natl. Acad. Sci. U.S.A.* **114**, E7348–E7357 (2017).
106. G. W. Carnell, K. A. Ciazynska, D. A. Wells, X. Xiong, E. T. Aguinam, S. H. McLaughlin, D. Mallery, S. Ebrahimi, L. Ceron-Gutierrez, B. Asbach, S. Einhauser, R. Wagner, L. C. James, R. Doffinger, J. L. Heeney, J. A. G. Briggs, SARS-CoV-2 spike protein stabilized in the closed state induces potent neutralizing responses. *J. Virol.* **95**, e0020321 (2021).
107. J. Zivanov, T. Nakane, S. H. W. Scheres, Estimation of high-order aberrations and anisotropic magnification from cryo-EM data sets in *RELION*-3.1. *IUCrJ* **7**, 253–267 (2020).
108. S. Q. Zheng, E. Palovcak, J. P. Armache, K. A. Verba, Y. Cheng, D. A. Agard, MotionCor2: Anisotropic correction of beam-induced motion for improved cryo-electron microscopy. *Nat. Methods* **14**, 331–332 (2017).
109. D. Tegunov, P. Cramer, Real-time cryo-electron microscopy data preprocessing with Warp. *Nat. Methods* **16**, 1146–1152 (2019).
110. A. Punjani, J. L. Rubinstein, D. J. Fleet, M. A. Brubaker, cryoSPARC: Algorithms for rapid unsupervised cryo-EM structure determination. *Nat. Methods* **14**, 290–296 (2017).
111. P. Emsley, B. Lohkamp, W. G. Scott, K. Cowtan, Features and development of Coot. *Acta Crystallogr. D Biol. Crystallogr.* **66**, 486–501 (2010).
112. R. T. Kidmose, J. Juhl, P. Nissen, T. Boesen, J. L. Karlsen, B. P. Pedersen, *Namdinator*—Automatic molecular dynamics flexible fitting of structural models into cryo-EM and crystallography experimental maps. *IUCrJ* **6**, 526–531 (2019).
113. P. V. Afonine, B. K. Poon, R. J. Read, O. V. Sobolev, T. C. Terwilliger, A. Urzhumtsev, P. D. Adams, Real-space refinement in PHENIX for cryo-EM and crystallography. *Acta Crystallogr. D Struct. Biol.* **74**, 531–544 (2018).
114. J. Buchrieser, J. Dufloo, M. Hubert, B. Monel, D. Planas, M. M. Rajah, C. Planchais, F. Porrot, F. Guivel-Benhassine, S. Van der Werf, N. Casartelli, H. Mouquet, T. Bruel, O. Schwartz, Syncytia formation by SARS-CoV-2-infected cells. *EMBO J.* **39**, e106267 (2020).

Acknowledgments: We acknowledge the staff at the Cryo-EM Facility of GIBH-CAS, SUST CryoEM, and Guangzhou Laboratory Bio-imaging Technology Platform for help with cryo-EM sample preparation and data collection. **Funding:** This work was supported by the National Natural Science Foundation of China (82341085 to X.X.); National Key Research and Development Program of China (2021YFA1300903 to X.X.); Emergency Key Program of Guangzhou Laboratory (EKPG21-06 to X.X.); R&D Program of Guangzhou Laboratory (SRPG22-002 to X.X.); Basic Research Project of Guangzhou Institutes of Biomedicine and Health, Chinese Academy of Sciences (GIBHBRP24-02 to X.X.); R&D Program of Guangzhou Laboratory (SRPG22-003 to J.H.); Natural Science Fund of Guangdong Province (2022A1515110211 to J.W.); Natural Science Fund of Guangdong Province (2022A1515110495

to B.L.); Young Doctoral Starting Sail Project of the Guangzhou Municipal Science and Technology Bureau (2024A04J4197 to J.W.); Young Doctoral Starting Sail Project of the Guangzhou Municipal Science and Technology Bureau (2024A04J4195 to B.L.); Young Doctoral Starting Sail Project of the Guangzhou Municipal Science and Technology Bureau (2024A04J4357 to Y.M.); and Grants from State Key Laboratory of Respiratory Diseases (SKLRD-Z-202515 to Y.M.). **Author contributions:** Conceptualization: X.X., J.W., Y.M., and X.C. Supervision: X.X., X.C., and Z.S. Data curation: J.W., Y.M., X.X., M.L., Y.L., Zexuan Li, and L.F. Investigation: J.W., Y.M., and X.X. Methodology: Zimu Li, X.X., J.W., Y.M., and H.Y. Project administration: X.X., J.W., and Y.M. Resources: X.X., X.C., Z.S., J.W., Y.M., M.S., M.L., and Y.L. Formal analysis: J.W., X.X., Y.M., B.L., and J.C. Validation: X.X., J.W., and Y.M. Visualization: X.X., J.W., M.Y., G.H., and H.Y. Writing—original draft: J.W., M.Y., and X.X. Writing—review and editing: J.W., M.Y., G.H., J.C., P.W., J.H., P.Z., X.C., Z.S., and X.X. **Competing interests:** The authors declare that they have no competing interests. **Data and materials availability:** Cryo-EM density maps and coordinates generated in this study have been deposited in the Electron Microscopy Data Bank (EMDB; https://www.ebi.ac.uk/emdb/) and the Protein Data Bank (PDB; https://www.rcsb.org/ with the following accession numbers: BtKY72 S-trimer: EMD-60551 and 8ZY0; BM48-31 S-trimer: EMD-60552 and 8ZY1; BANAL-20-52 S-trimer: EMD-60553 and 8ZY2; BANAL-20-236 S-trimer: EMD-60554 and 8ZY3; YN2013 S-trimer: EMD-60555 and 8ZY4; RmYN02 S-trimer: EMD-60556 and 8ZY5; GX2013 S-trimer: EMD-60557 and 8ZY6; HeB2013 S-trimer: EMD-60558 and 8ZY7; dimeric BtKY72-RBD:bACE2$_{Ra9479}$ complex: EMD-60559 and 8ZY9; and monomeric BtKY72-RBD:bACE2$_{Ra9479}$ complex: EMD-60560 and 8ZYA. All data needed to evaluate the conclusions in the paper are present in the paper and/or the Supplementary Materials.

Submitted 19 July 2024
Accepted 7 February 2025
Published 14 March 2025
10.1126/sciadv.adr8772